JGR Oceans

Key Points:

- Rhythms of the Agulhas Current, acceleration, and meanders on the synoptic scale were studied from a new energetic anisotropy perspective
- Agulhas Current meanders can be generated either by local anticyclone-mean flow interactions or upstream cyclone merging
- Balance between eddy anisotropy and mean flow strain decides meander growth, with broader applications to other western current systems

Correspondence to:

X.-Y. Yang and D. Wang,
xyyang@xmu.edu.cn;
dxwang@mail.sysu.edu.cn

Author Contributions:

Conceptualization: Xin Guo, Xiao-Yi Yang, Dongxiao Wang
Data curation: Xin Guo, Xiao-Yi Yang
Formal analysis: Xin Guo
Funding acquisition: Xiao-Yi Yang
Investigation: Xin Guo, Xiao-Yi Yang
Methodology: Xin Guo, Xiao-Yi Yang, Qiang Deng, Hongyang Lin
Project administration: Xiao-Yi Yang
Software: Xin Guo
Supervision: Xiao-Yi Yang
Validation: Xiao-Yi Yang, Dongxiao Wang
Visualization: Xin Guo, Xiao-Yi Yang, Dongxiao Wang
Writing – original draft: Xin Guo
Writing – review & editing: Xiao-Yi Yang, Qiang Deng, Hongyang Lin, Dongxiao Wang

Rhythms of the Agulhas Current Within the Framework of Energetic Anisotropy

Xin Guo[1] , Xiao-Yi Yang[1,2] , Qiang Deng[1], Hongyang Lin[1] , and Dongxiao Wang[2,3]

[1]State Key Laboratory of Marine Environmental Science, College of Ocean and Earth Sciences, Xiamen University, Xiamen, China, [2]Southern Marine Science and Engineering Guangdong Laboratory (Zhuhai), Zhuhai, China, [3]School of Marine Sciences, Sun Yat-Sen University, Guangzhou, China

Abstract This study investigates the mechanisms driving the acceleration and meandering of the Agulhas Current (AC), focusing on the role of eddy-mean flow interactions. The analysis revealed that anticyclones originating from the Mozambique Channel and south of Madagascar played pivotal roles in accelerating the AC. Simultaneously, when anticyclones collide with the AC, they undergo processes of rotating and elongating into ellipses. In addition to the previously suggested barotropic instability induced by anticyclones, this study revealed that the merging of cyclones with the AC plays a role in the generation of meanders. Upstream cyclones reduce the horizontal potential vorticity gradient, facilitating eddies to traverse the current. The AC envelops these cyclones and flows in meandering patterns. The places where these meanders form are not exclusive to the Natal Bight. In addition, we further diagnose the kinetic energy conversion to reveal the interaction between eddy anisotropy (i.e., eddy deformation and orientation) and mean flow strain (i.e., stretching and shearing). The results suggest that the anisotropy of anticyclonic and cyclonic eddies prompts downscale KE transfer and the growth of meanders, establishing a positive feedback loop. Contrary to the findings of previous hypotheses, the acceleration of AC in turn leads to a decrease in the mean flow strain rate, exerting negative feedback on energy conversion and inhibiting the development of meanders. These two feedback mechanisms work together to determine the fate of AC meandering. The energetic anisotropy diagnosis holds potential applicability to other western boundary current systems.

Plain Language Summary The Agulhas Current (AC) is the strongest western boundary current in the Southern Hemisphere. The variabilities in its strength and meandering behavior influence the local marine environment and meridional heat transport. This research is devoted to investigating the mechanisms behind the acceleration and formation of meandering. We find that the acceleration in AC is attributed to upstream anticyclones because the velocities of these anticyclones align with the mean flow in their interaction area. Additionally, this study first demonstrates that nonlocal cyclones can reduce the barrier of the horizontal potential vorticity gradient. These cyclones thus cross the current, causing the AC to form a pulse-like meandering flow. Meandering also occurs locally due to the barotropic instability of the AC, indicating a downscaled conversion of kinetic energy. We employ a diagnosis of the kinetic energy budget, highlighting the significant influence of eddy anisotropy, including the squeezing of anticyclones and the growth of cyclones. However, the acceleration of the AC would reduce its strain, which abates the original barotropic instability.

1. Introduction

As the strongest western boundary current in the Southern Hemisphere, the Agulhas Current (AC) flows southwestward along the eastern coast of South Africa, transporting a large amount of warm and saline water poleward (Bryden et al., 2005; Lutjeharms, 2007). The Agulhas Current feeds an interbasin water mass exchange between the Indian Ocean and the Atlantic Ocean and is a key component of global ocean circulation (Backeberg et al., 2012; Beal et al., 2011; Gordon, 1986; van Sebille et al., 2010).

The AC originates from the interior gyre circulation as well as from upstream regions, that is, the Mozambique Channel (MC) and East Madagascar Current (EMC), primarily in the form of mesoscale eddies. Several studies have estimated AC transport at different sites, with values ranging from 69.7 ± 21.5 Sv at 31–32°S (Bryden & Beal, 2001; Bryden et al., 2005) to 84 ± 11 Sv at 34°S (Beal et al., 2015). Although its path typically remains stable from the Natal Bight at approximately 28°S to Gqeberha (formerly known as Port Elizabeth) at approximately 34°S, probably due to the steep bottom topography (Gründlingh, 1983; Lutjeharms, 2006), the AC

sometimes veers offshore in the form of a meandering flow. These meanders are often referred to as Natal Pulses (Lutjeharms & Roberts, 1988) and are likely to contribute to inshore upwelling (Leber & Beal, 2015; Leber et al., 2017) and the shedding of Agulhas rings downstream (Backeberg et al., 2008; Russo et al., 2021; van Aken et al., 2013; van Leeuwen et al., 2000), although their effect on interbasin exchange is limited (Elipot & Beal, 2015).

Increased meandering within the AC over time has been observed using moorings, while total transport remains stable (Beal & Elipot, 2016). This raises the question of how meanders affect the current's strength and meridional fluxes. To address this, our study seeks to unravel the intricate relationship between the AC strength and its meanders. Anomalies in AC transport during meanders vary greatly among different studies, from an increase (Biastoch et al., 2009) to a decrease of 15–25 Sv (Bryden et al., 2005), or even remaining almost unchanged (Leber & Beal, 2014). It is worth emphasizing that volume transport is an integral variable involving the velocity, width, and vertical structure of the flow. These variables are prone to exhibiting incoordinate variations in a dynamic western boundary current system. For example, when the AC broadens and its core velocity decreases concurrently, the overall transport changes insignificantly, as reported by Leber and Beal (2014). The changes in the velocity distribution and dynamic structure of the AC may not be readily discernible when solely focusing on transport. Therefore, it is necessary to analyze the flow velocity, width, and vertical structure of the AC separately. Examining the relationships among these components and the AC meanders also aids in understanding the mechanisms underlying the variability in the dynamic western boundary current system. Accordingly, we explore AC variability from two perspectives, that is, strength associated with flow velocity and meanders. The intrinsic connection between these two aspects and their effect on the future evolution of the AC are the motivation of this study.

Mesoscale eddies from upstream MC and EMC exert great impacts on AC variability. Both anticyclonic and cyclonic eddies propagate from these upstream regions toward the AC (Backeberg et al., 2008; Quartly et al., 2006; H. Ridderinkhof et al., 2010; de Ruijter et al., 2004; Stramma & Lutjeharms, 1997), affecting it in two primary ways. First, these eddies impact the strength of the AC. In situ measurements revealed that offshore eddies could drive substantial transport variability (Casal et al., 2009). Braby et al. (2016) showed that anticyclones from the MC and the EMC prompt the acceleration of the current core at 30°S, whereas cyclones tend to decelerate the AC. Second, upstream eddies play a critical role in AC meandering. Several studies have traced AC meandering back to propagating features in the MC and the EMC and beyond (de Ruijter et al., 1999; Elipot & Beal, 2015). A numerical study by Biastoch et al. (2008) further demonstrated the indispensable effect of the Mozambique eddies on AC meander development. Various studies on the energy budget show that barotropic instability is the primary engine driving the meandering behavior of the AC (Elipot & Beal, 2015; van der Vaart & de Ruijter, 2001). However, the role of baroclinic instability in AC meanders is yet to be quantified using observations. Anticyclonic and cyclonic eddies likely affect the AC meanders in distinct ways. Some studies suggest the barotropic instability associated with meanders is linked to offshore anticyclonic eddies (Tsugawa & Hasumi, 2010; Yamagami et al., 2019), probably by increasing the flow speed (de Ruijter et al., 1999). In addition, cyclones originating from upstream regions can also induce AC meandering (Yamagami et al., 2019). Statistical analysis suggests that the entrainment of cyclones may sometimes cause larger meanders than those induced by anticyclones (Braby et al., 2016). Furthermore, a previous study noted that cyclonic eddies interacting with the AC are sometimes accompanied by anticyclones (Braby et al., 2016), yet the impact of these dipole eddy pairs on the AC's strength and path is less understood. In summary, both anticyclones and cyclones can induce meanders in the AC; however, anticyclones are typically associated with acceleration, while cyclones tend to cause deceleration. This distinct relationship between the AC's strength and meanders during eddy-mean flow interaction remains to be clarified.

Increased meandering within the AC over time (Beal & Elipot, 2016) underscores the need for research into the strength of the AC and its associated meanders. Despite the established influence of both cyclone and anticyclone eddies on the AC variability, there remains a gap in understanding how these eddies of different polarities interact with the AC in distinct ways, potentially leading to various relationships between its strength and path. This study aims to probe the physical mechanisms accounting for variations in the strength and meandering behavior of the Agulhas Current, specifically focusing on their relationship with different types of mesoscale eddies.

2. Data and Methods

2.1. Data

Satellite altimeter data are used to quantify accelerations and meanders of the Agulhas Current and detect mesoscale eddies. To further examine the eddy-mean flow interaction, higher resolution reanalysis data are also employed in this study.

The daily gridded L4 satellite altimetry data set was obtained from the Copernicus marine environment monitoring service (CMEMS) and the Copernicus Climate Change Service (C3S) (https://cds.climate.copernicus.eu/). This data set comprises various parameters, including absolute dynamic topography (ADT), absolute geostrophic velocity, sea level anomaly (SLA), and geostrophic velocity anomalies relative to a 20-year mean reference period (1993–2012) with a horizontal resolution of 0.25° and a time span of 27 years from January 1993 to June 2020.

The Mercator Ocean global reanalysis (GLORYS) product was also obtained from the CMEMS. The data sets provide global ocean eddy-resolving reanalysis data, including 11 variables displayed on a standard regular grid with spatial resolutions of 1/12° and 50 standard levels. Russo et al. (2022) illustrated that the GLORYS reanalysis data set is one of the top-performing data sets, particularly in the Agulhas System, when compared to the Commonwealth Scientific and Industrial Research Organization's Bluelink Reanalysis and the Fleet Numerical Meteorology and Oceanography Center's Global Hybrid Coordinate Ocean Model reanalysis. Daily data sets of potential temperature, salinity, sea surface height above the geoid (SSH), and horizontal velocity from January 1993 to June 2020 are utilized here. The average patterns of SSH and velocity fields from the GLORYS data set closely resemble the average ADT and velocity fields from satellite altimetry.

2.2. Methods

2.2.1. Potential Vorticity

Shi et al. (2021) found that cyclonic eddies can cross the current by reducing the horizontal potential vorticity (PV) gradient. To examine the interaction between cyclones and the AC, we calculate PV using the following equation:

$$\text{PV} = \frac{f + \zeta}{\rho} \frac{\partial \rho}{\partial z} \tag{1}$$

where f and ζ are the planetary and relative vorticities, respectively, and ρ is the potential density.

2.2.2. Energy Conversion Rate

According to previous studies, mesoscale eddy activity in an AC system is primarily regulated by kinetic energy conversion (referred to as KmKe1) (de Ruijter et al., 1999; Tsugawa & Hasumi, 2010; Zhu et al., 2018). We applied a temporal filter to separate the velocity variables into AC flow and mesoscale eddy velocities. In contrast to the Reynolds decomposition method, where the mean flow is defined as a temporal average, our western boundary current obtained via low-pass filtering varies over time. This allows us to analyze the feedback of background flow during the interaction process with mesoscale eddies. We compute KmKe1 as follows (Tsugawa & Hasumi, 2010; Zhu et al., 2018):

$$KmKe1 = -\left[\overline{u'u'}\,\overline{\frac{\partial \langle u \rangle}{\partial x}} + \overline{u'v'}\left(\overline{\frac{\partial \langle u \rangle}{\partial y}} + \overline{\frac{\partial \langle v \rangle}{\partial x}}\right) + \overline{v'v'}\,\overline{\frac{\partial \langle v \rangle}{\partial y}} \right] \tag{2}$$

where u' and v' denote the 200-day high-pass filtered zonal and meridional velocity anomalies capturing the mesoscale eddy signals, respectively, and $\langle u \rangle$ and $\langle v \rangle$ are the low-pass filtered signals representing the background horizontal currents. The overbar denotes a 9-day running mean, chosen as the average time span of acceleration events defined in the next section. A positive KmKe1 value denotes barotropic instability within the slowly varying background flow system and kinetic energy transfer from the background current to eddies, and vice versa. The choice of 200-day cutoff for filtering aligns with previous studies. They also set the cutoff period

to not less than 200 days in the AC system (Adeagbo et al., 2022; Backeberg et al., 2012; Zhu et al., 2018). To test the impact of the 200-day cutoff period on the results, we also applied other filtering cutoffs, such as 120 days, 90 days, and 60 days. When the 60-day cutoff period is applied, the eddy signals cannot be clearly distinguished from the background flow. Although mean flow changes may be underestimated when the 200-day truncation was applied, the results of the 120-day and 90-day filtering cutoffs are highly consistent with those of the 200-day cutoff, both in terms of spatial pattern and temporal variation.

The contribution of potential energy conversion to meanders and accelerations of the AC can be quantified as

$$\text{PmPe1} = \frac{\text{g}}{\overline{\rho}d\tilde{\rho}/dz}\left[\overline{u'\rho'}\frac{\overline{\partial\langle\rho\rangle}}{\partial x} + \overline{v'\rho'}\frac{\overline{\partial\langle\rho\rangle}}{\partial y}\right] \tag{3}$$

where ρ' and $\langle\rho\rangle$ denote the 200-day high-pass and low-pass filtered potential density, and $\tilde{\rho}(z)$ is the temporal and horizontal mean potential density. A positive PmPe1 value denotes baroclinic instability within the slowly varying background flow and potential energy transfer from the background current to eddies.

2.2.3. Anisotropy Decomposition

Further decomposition of the energy conversion is necessary to understand the feedback mechanisms between eddies and the AC in detail. With reference to the theoretical foundation of variance ellipse analysis, the eddy momentum flux tensor can be separated into isotropic and anisotropic parts (Waterman & Hoskins, 2013; Waterman & Lilly, 2015). The equation for this decomposition is as follows:

$$\begin{bmatrix} \overline{u'u'} & \overline{u'v'} \\ \overline{u'v'} & \overline{v'v'} \end{bmatrix} = \begin{bmatrix} K & 0 \\ 0 & K \end{bmatrix} + \begin{bmatrix} M & N \\ N & -M \end{bmatrix}$$

where $K = \frac{\overline{u'^2} + \overline{v'^2}}{2}$ is the eddy kinetic energy (EKE) and $M = \frac{\overline{u'^2} - \overline{v'^2}}{2}$ and $N = \overline{u'v'}$ describe the deformation and orientation of eddies at a given point, respectively, implying local anisotropy (i.e., a tendency to align along a preferred axis). The orientation of the preferred axis (i.e., anisotropic orientation) is calculated by

$$\theta_a = \frac{1}{2}arctan\left(\frac{N}{M}\right) = \frac{1}{2}arctan\left(\frac{2\overline{u'v'}}{\overline{u'^2} - \overline{v'^2}}\right) \tag{4}$$

The combination of M and N is represented as L:

$$L = \sqrt{M^2 + N^2} = \frac{1}{2}\sqrt{\left(\overline{u'^2} - \overline{v'^2}\right)^2 + 4\left(\overline{u'v'}\right)^2} \tag{5}$$

Therefore, $M = Lcos2\theta_a$ and $N = Lsin2\theta_a$. L is not greater than the total eddy kinetic energy K. A value of L close to 0 implies that the average eddy motion is locally isotropic, while a value of L close to K suggests high anisotropy with local extension along the preferred axis and compression along a minor axis. Therefore, L characterizes the portion of EKE associated with anisotropic variability (Stewart et al., 2015).

Following the methodology of Qiao et al. (2023), KmKe1 can be further decomposed into isotropic and anisotropic production components:

$$
\begin{aligned}
KmKe1 &= -sum\left\{ \begin{bmatrix} \overline{u'u'} & \overline{u'v'} \\ \overline{u'v'} & \overline{v'v'} \end{bmatrix} \odot \begin{bmatrix} \overline{\dfrac{\partial \langle u \rangle}{\partial x}} & \overline{\dfrac{\partial \langle u \rangle}{\partial y}} \\ \overline{\dfrac{\partial \langle v \rangle}{\partial x}} & \overline{\dfrac{\partial \langle v \rangle}{\partial y}} \end{bmatrix} \right\} \\
&= -\frac{1}{2}sum\left\{ \left(\underbrace{\begin{bmatrix} K & 0 \\ 0 & K \end{bmatrix}}_{isotropy} + \underbrace{\begin{bmatrix} M & N \\ N & -M \end{bmatrix}}_{anisotropy} \right) \odot \left(\underbrace{\begin{bmatrix} Div & -\zeta \\ \zeta & Div \end{bmatrix}}_{isotropy} + \underbrace{\begin{bmatrix} S_n & S_s \\ S_s & -S_n \end{bmatrix}}_{anisotropy} \right) \right\} \\
&= \underbrace{-K \cdot Div}_{isotropy\ production} \quad \underbrace{-\{L cos 2\theta_a S_n + L sin 2\theta_a S_s\}}_{anisotropy\ production}
\end{aligned}
\tag{6}
$$

where $Div = \left(\overline{\dfrac{\partial \langle u \rangle}{\partial x}} + \overline{\dfrac{\partial \langle v \rangle}{\partial y}} \right)$ and $\zeta = \left(\overline{\dfrac{\partial \langle v \rangle}{\partial x}} - \overline{\dfrac{\partial \langle u \rangle}{\partial y}} \right)$ are the divergence and relative vorticity of the mean flow, respectively; and $S_n = \overline{\dfrac{\partial \langle u \rangle}{\partial x}} - \overline{\dfrac{\partial \langle v \rangle}{\partial y}}$ and $S_s = \overline{\dfrac{\partial \langle v \rangle}{\partial x}} + \overline{\dfrac{\partial \langle u \rangle}{\partial y}}$ are the normal (stretch) and shear components of the mean flow strain rate S, respectively. The strain rate is calculated by

$$
S = \sqrt{S_n{}^2 + S_s{}^2} = \sqrt{\left(\overline{\dfrac{\partial \langle u \rangle}{\partial x}} - \overline{\dfrac{\partial \langle v \rangle}{\partial y}} \right)^2 + \left(\overline{\dfrac{\partial \langle v \rangle}{\partial x}} + \overline{\dfrac{\partial \langle u \rangle}{\partial y}} \right)^2}
\tag{7}
$$

The maximum stretching direction of mean flow is given by the principal axis of the strain rate tensor (Gula et al., 2014; Zhang et al., 2019):

$$
\theta_s = \frac{1}{2}\arctan\left(\frac{S_s}{S_n} \right)
\tag{8}
$$

For a mean flow without external sources or sinks, the anisotropy production component dominates the energy conversion in Equation 6. Thus, KmKe1 can be approximated as follows:

$$
KmKe1 \cong -\vec{L} \cdot \vec{S} = -LS cos 2\alpha
\tag{9}
$$

where $\vec{L} \triangleq (M, N)$ is a vector term relating to eddy anisotropy, with magnitude of L and orientation of $2\theta_a$. $\vec{S} \triangleq (S_n, S_s)$ represents the mean flow strain with its magnitude of the strain rate S and orientation of $2\theta_s$. The orientations of $\vec{L}$ and $\vec{S}$ are decided by the relative dominance between their own two components. The relative angle between $\vec{L}$ and $\vec{S}$ is defined as 2α, where $\alpha = \theta_a - \theta_s$. According to Equation 9, the barotropic instability dominated by its anisotropic production component can be interpreted as the projection of $\vec{L}$ in a "strain" co-ordinate system. Therefore, the direction of KmKe1 is sensitive to the relative direction 2α. A positive cascade occurs when the eddy anisotropy $\vec{L}$ is in the contrary direction to the mean flow strain $\vec{S}$ (i.e., $2\alpha = 180°$). The magnitude of KmKe1 change is primarily determined by the slowly varying mean flow strain rate S and the eddy kinetic energy associated with anisotropy L. This decomposition of KmKe1 provides additional insights into the typical eddy structural characteristics and their interactions with the mean flow strain.

3. Statistical Features of AC Acceleration

The AC flows southwestward along the African continent and enhances gradually downstream (Figure 1a). The maximal flow velocity can reach up to 1.40 m/s, which is approximately 0.4 m/s smaller than the observations from moorings (Beal et al., 2015). The AC core, characterized by the maximum speed, becomes more stable at Port Edward (located at approximately 31°S), as depicted by the white bars in Figure 1a. The steep topography in this region makes it an ideal location for investigating the strength of the AC and its variability (Beal & Bryden, 1999; Bryden et al., 2005; Gründlingh, 1983; Schumann, 1981).
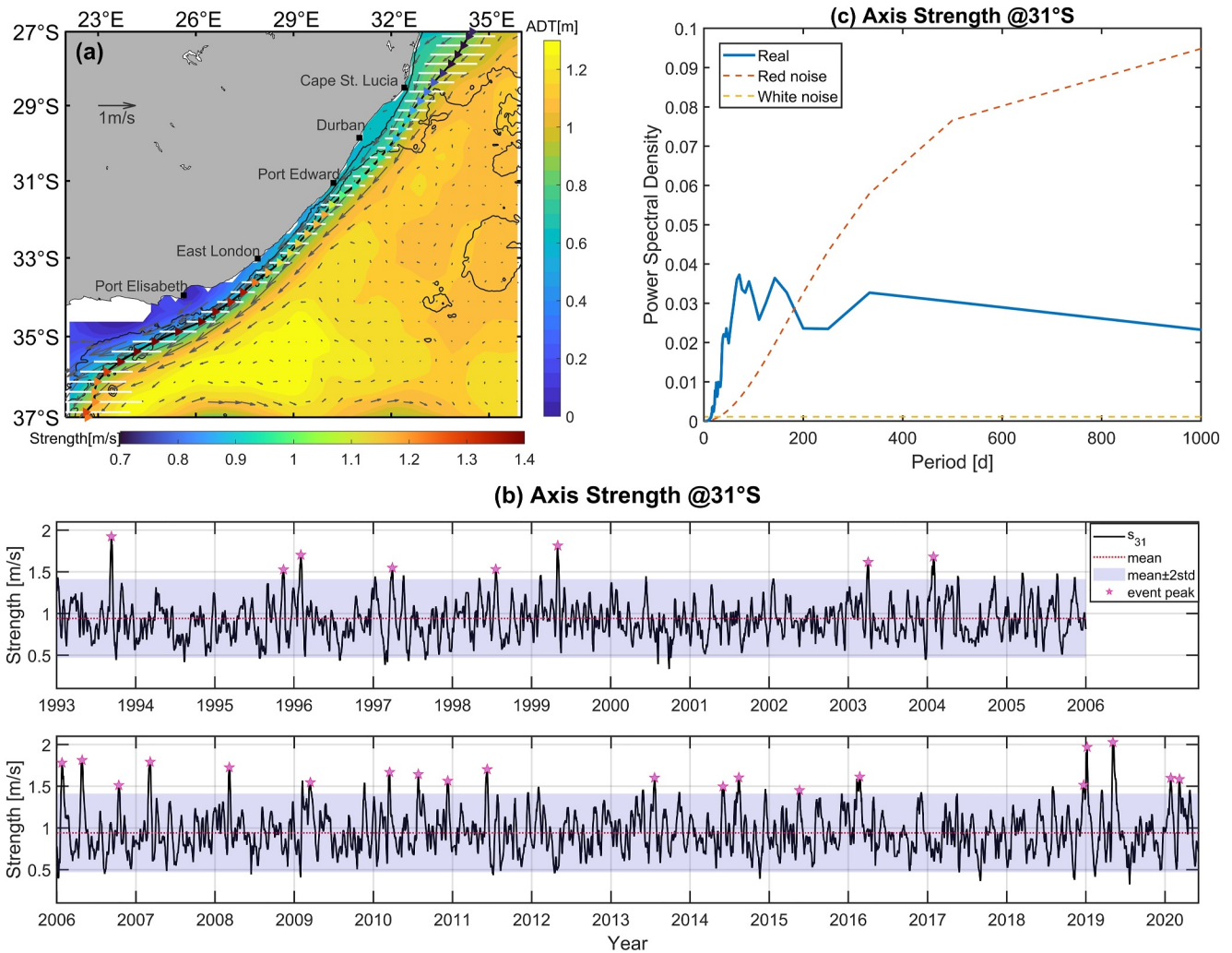
Figure 1. (a) Climatology of the absolute dynamic topography (ADT) along with the associated geostrophic flow from 1993 to 2020. The path of the Agulhas Current (AC) core is indicated by the bold black line with white bars representing the standard deviation (std) of the current core location and colored triangles representing its strength (unit: m/s) at the respective latitudes. Thin black contours are the 500 and 2,000 m isobaths. (b) Time series of the AC strength at 31°S. The red dashed line and the purple shadow denote the mean and ±2std, respectively. The pink pentagrams designate the peaks of each acceleration event identified in the text. (c) The power spectrum of the AC strength at 31°S. The red and yellow dashed lines denote the red and white noise, respectively.

The daily time series of AC intensity at Port Edward, defined as the maximum speed, has a mean value of 0.94 m/s and a standard deviation (std) of 0.24 m/s (Figure 1b). The distribution of anomalies has a skewness of 0.60, with acceleration events being stronger than deceleration events. The analysis of the power spectrum (Figure 1c) indicates that the high-frequency component of the AC strength with periods shorter than 200 days is significant. This dominant period coincides with the average lifespan of mesoscale eddies in the ocean (Chelton et al., 2011; Zhu et al., 2018), alluding to the influence of mesoscale eddies on the variability in AC strength. To further examine the pronounced acceleration of the AC core, a total of 28 acceleration events are identified from the daily time series of AC strength. These events are selected based on the criterion that the core intensity remains above two standard deviations for more than five consecutive days. The peaks of each acceleration event are marked by pink pentagrams in Figure 1b. The average duration of these events is 10.4 days, with a mean strength reaching 1.58 m/s.

Both the satellite data and the GLORYS reanalysis data show composite elongated anticyclonic circulation and a weaker cyclone straddling the AC path in association with the AC acceleration events (Figures 2a and 2b). Along the zonal section, a positive-negative-positive sandwich pattern of meridional velocity anomalies extends from the surface to a depth of approximately 1000 m, manifesting the quasi-barotropic structure of the vortex pair
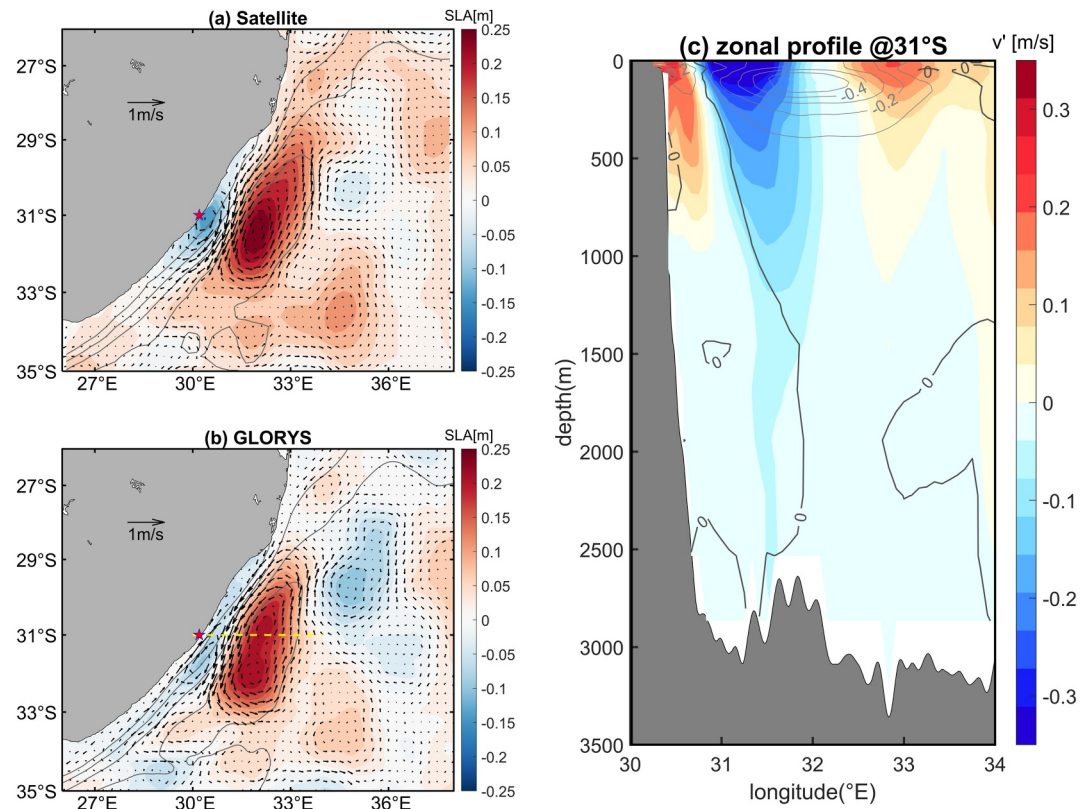
Figure 2. Composites of the sea level anomaly (SLA) and geostrophic flow anomalies during 28 acceleration event peaks utilizing data from satellite altimetry (a) and GLORYS reanalysis (b). The gray contours represent the ADT and SSH, respectively. The pentagrams and yellow dashed line depict the zonal section along the referenced latitude of 31°S. (c) Composites of the meridional velocity anomaly along the 31°S zonal section during the event peaks. The gray contours represent potential density anomalies (kg/m^3).

(Figure 2c). The negative anomalies are more pronounced and deeper than the positive anomalies, possibly owing to the entrainment of the anticyclone into the western boundary current. Additionally, negative (positive) potential density anomalies are observed within the anticyclone (cyclone) scope. This signifies a seesaw-like vertical displacement of isopycnals with depression (uplift) on the offshore (inshore) flank of the AC, which is consistent with the convergence (divergence) effect of mesoscale eddies.

Positive EKE anomalies are observed in the upstream regions before the AC acceleration events (Figure 3a). The maximum EKE value arises in the MC region at approximately 40–110 days and in the EMC region at approximately 50–70 days prior to the events, implying propagation speeds of 17 km/day. These are similar with previous studies (Elipot & Beal, 2015; Schouten et al., 2003) and the results of eddy tracks (mentioned below).

To further verify the association between AC acceleration and eddies originating from upstream regions, we conducted a water mass analysis in the peripheral area of the AC (the four boxes in Figure 3a). The T-S diagrams exhibit the average temperature and salinity properties of the AC (dashed line in Figure 3b), as reported by previous studies (Beal & Bryden, 1999; Beal et al., 2006); these values are largely consistent with those of two upstream regions (blue and orange lines) and the recirculation of the southern Indian Ocean subtropical gyre (RA, green line). The relatively fresher MC and EMC water masses mixed with the saltier recirculation water supplement the AC and maintain the mean AC water properties somewhere in between. During the AC acceleration peaks, however, the properties of AC deviate from the average and exhibit a closer resemblance to those of the upstream regions, particularly for water masses lighter than 26.5 kg/m^3 (gray dots in Figure 3b). We employ a two-dimensional Kolmogorov-Smirnov test and permutational multivariate analysis of variance. The results from both methods indicate significant deviations of the accelerating AC from climatology.
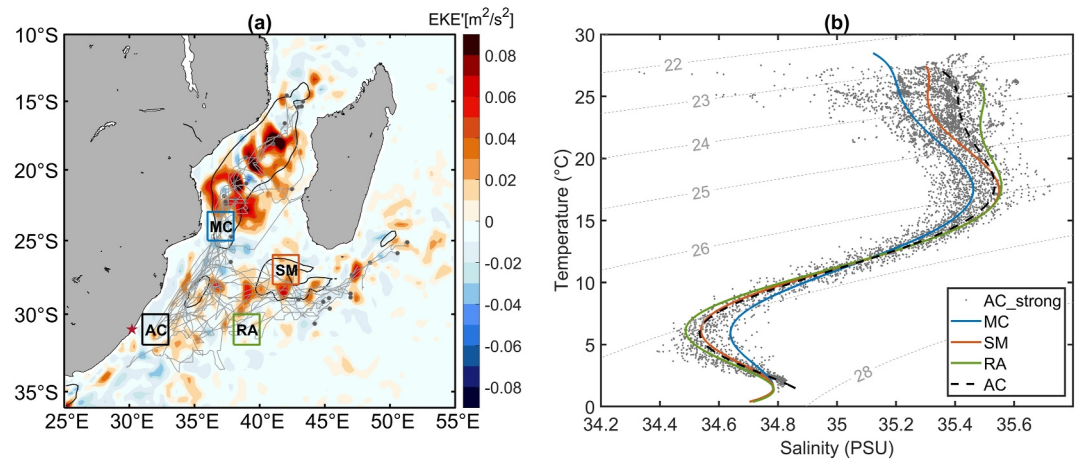
Figure 3. (a) Composite eddy kinetic energy (EKE, color shading) anomalies 60 days before the acceleration peaks. The thick black contours enclose the regions with climatological EKE values exceeding 0.09 m²/s². The gray lines represent the trajectories of anticyclones associated with the events. The pentagram depicts the Port Edward. The four boxes mark the key regions for water mass analysis in Figure 3b, that is, the Mozambique Channel (MC) region at 36–38°E, 23–25°S; the southern tip of Madagascar (SM) region at 41–43°E, 26–28°S; the AC region at 31–33°E, 30–32°S; and the recirculation region (RA) at 38–40°E, 30–32°S. (b) The temperature-salinity (T-S) diagram. The lines denote the average T-S relationships in the four regions. The gray dots denote the T-S relationships in the AC region during the event peaks.

Then, we examined the 28 events one by one, identifying the local extrema of SLA and tracking the anticyclonic (cyclonic) eddies by anomalously convex (concave) SSH around their centers. Almost all events (with only one exception) are accompanied by anticyclonic eddies on the offshore flank, while on the inshore flank, cyclonic eddies emerge for more than half of the events. The trajectories of the anticyclones are consistent with previous studies (Elipot & Beal, 2015; Schouten et al., 2002). Of the 28 events, 15 were traced back to the MC, 11 to the EMC, and 1 to the intersection region between them. The mean propagation speed in upstream regions is approximately 6 km/day, which is in line with the typical transmission speed of mesoscale eddies (Chelton et al., 2011; de Ruijter et al., 2004; Schouten et al., 2003). In contrast, the eddy transmission speed in the AC region can be up to 19.4 km/day, similar to the previous study (Elipot & Beal, 2015), probably owing to the advection of the western boundary current.

Next, we detail the interaction of composite anticyclones with the AC (Figure 4). An intact anticyclone can be clearly detected as early as approximately 45 days before the event peaks, centered near 35.5°E, 28.5°S (Figure 4a). Then, the ellipse elongates with its major axis parallel to the AC direction as it moves closer to the AC (Figure 4b). Approximately 15 days before the peaks (Figure 4c), the intensified anticyclone impinged onto the AC, with its edge encountering the eastern flank of the jet. Subsequently (Figure 4d), the elliptical anticyclone further entrains into the AC, with its velocities aligning with the AC flow. At the peak of the events (Figure 4e), the anticyclone centers east of the AC at 31°S and further squeezes the main flow, leading to a significant acceleration of the AC. Thereafter, the anticyclone moves southwestward with the AC and gradually decays until it finally merges into the AC retroflection system (Figure 4f). The average SLA and EKE within the anticyclones initially increase and then decrease (not shown).

4. The Generation of AC Meandering During Acceleration

In addition to the squeezing and deformation of the offshore anticyclone, a weak but distinct inshore cyclonic circulation emerges at the peak phase of AC acceleration (Figures 4d and 4e). It tends to be advected downstream (Figure 4f), signifying the growth and migration of the AC meander (Elipot & Beal, 2015; Lutjeharms et al., 2003). To determine the connection between AC meandering and acceleration, 17 meandering cases are sorted out of the total 28 acceleration events, while the other 11 cases exhibit a merely straight jet with the anticyclone elongated northeast–southwest along the jet axis (Figure 5a). The absence of inshore cyclones in these 11 cases is analyzed below within the framework of energy anisotropy. Additionally, the relatively poor performance of altimeters near the coast introduces some uncertainty in detecting inshore cyclones. By tracking the inshore cyclonic anomalies, these 17 acceleration and meandering events can be further grouped into upstream
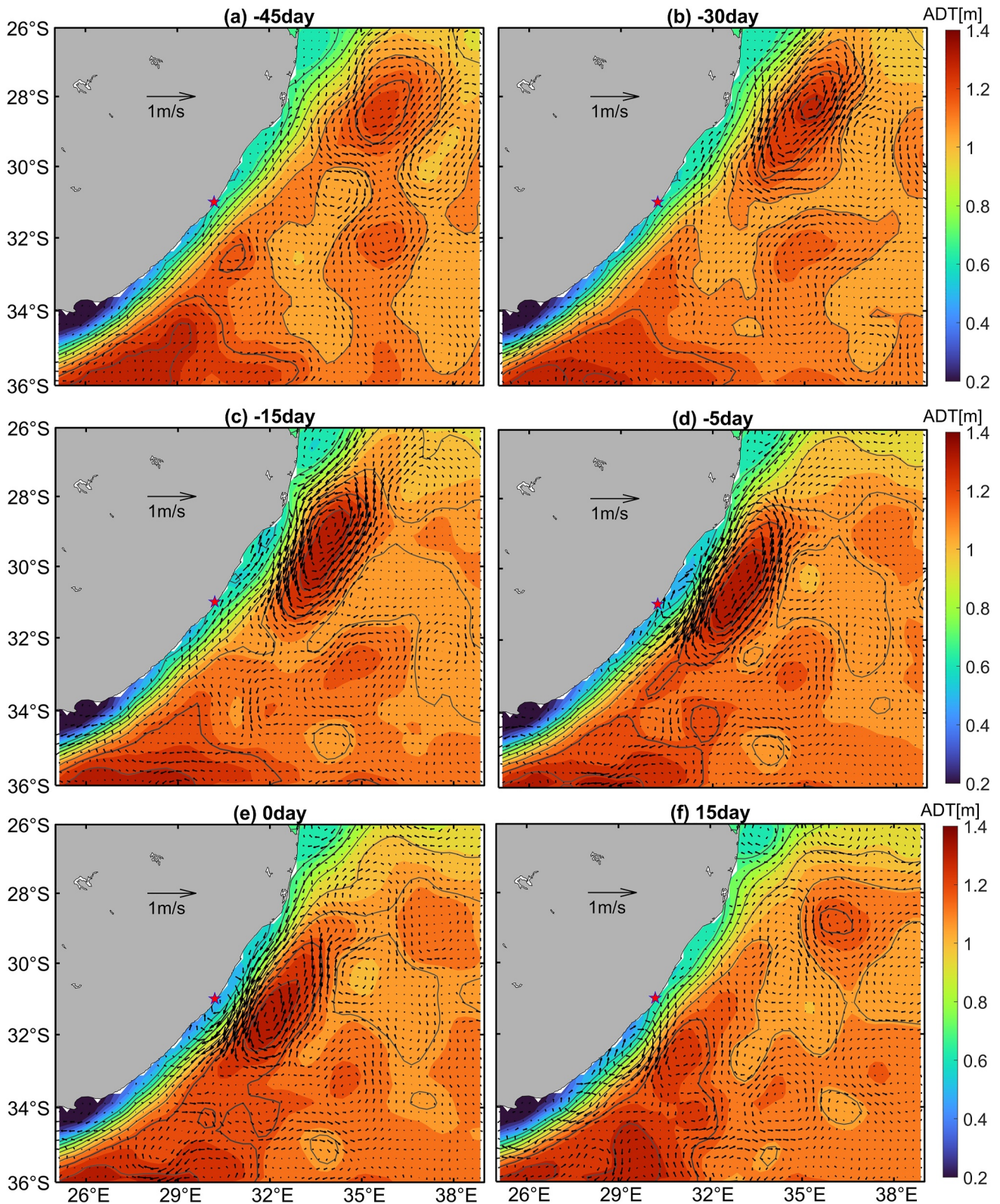
Figure 4. Composite of ADT (color shadings) and geostrophic velocity anomalies (vectors) before and after the acceleration event peaks. The black contours mark the composite ADT values with a contour interval of 0.1 m, with 0.8 and 1.2 m contours highlighted in bold. The pentagrams indicate the Port Edward.
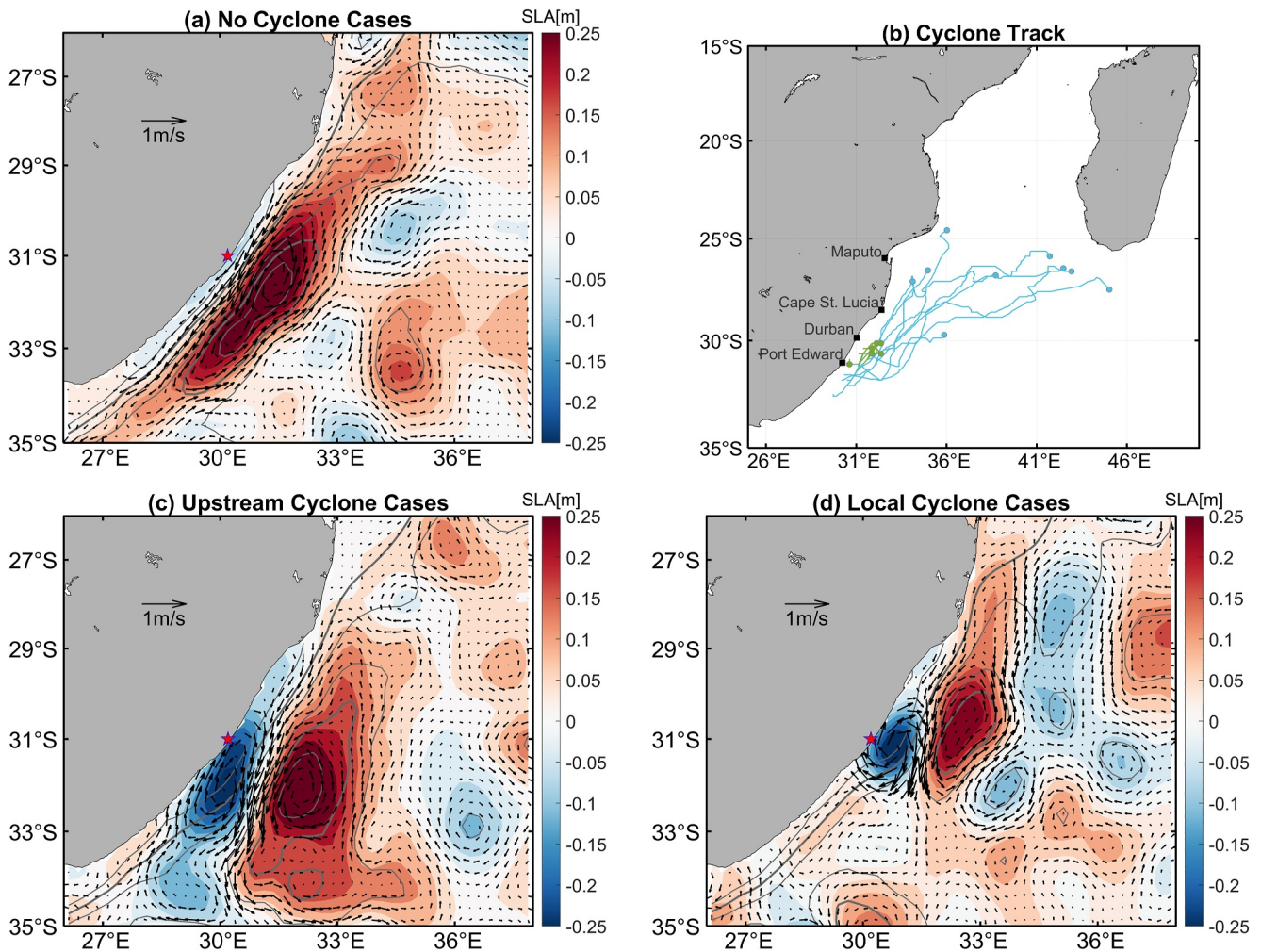
Figure 5. (a) Composites of sea level anomalies (SLAs, color shadings) and geostrophic flow anomalies (vectors) during the peak of no cyclone cases. The gray contours represent the composite ADT, with 0.8 and 1.3 m contours highlighted in bold. (b) Trajectories of cyclones associated with acceleration events. The blue and green lines represent the cyclones originating from the upstream region and local region, respectively. (c–d) Same as in (a) but for upstream cyclone cases and local cyclone cases.

cyclone cases (9 cases with blue trajectories in Figure 5b) and locally generated cyclone cases (8 cases with green trajectories in Figure 5b). Local cyclones predominantly originate within the range between Durban and Port Edward. Upstream cyclones exhibit rather diverse motion trajectories, tracing back to the MC, and south of Madagascar or northeast of the AC. The cyclones originating from the MC may form near Delagoa Bay (at Maputo) due to the interaction between anticyclones and the winding coastline (Cossa et al., 2016), while those from south of Madagascar are probably rooted in the separating EMC and appear as dipole-like vortex pairs with anticyclones (W. Ridderinkhof et al., 2013; de Ruijter et al., 2004). The observation of other upstream cyclones suggests their possible origin from the splitting of cyclones or the shearing of two anticyclones.

The composite SLA for the upstream cyclone cases (Figure 5c) reveals vortex pair centers south of the Port Edward, implying that the meander precedes the acceleration in these cases. For the local cyclone cases (Figure 5d), the vortex pair occurs exactly at a latitude near Port Edward with a smaller size. Moreover, the composite cyclonic anomalies in both groups propagated downstream to the south of Gqeberha at a speed of approximately 10.8 km/day. This is consistent with the characteristics of AC meanders, which have a speed of 10–20 km/day estimated by previous studies (de Ruijter et al., 1999; Lutjeharms & Roberts, 1988). The interaction processes with the AC may significantly vary for cyclones from different sources. Therefore, we analyzed these two groups separately.

Given the diversity of upstream cyclone trajectories, their evolution and interaction with the mean flow may vary case by case. Here, we select the second (hereafter C2) and fourth (hereafter C4) acceleration events as representative examples to demonstrate their similarities and differences (Figure 6), with acceleration peaks occurring on 1995-11-13 and 1997-03-29, respectively. Approximately 45 days prior to the event peaks, a cyclone emerges north of 30°S in both cases (Figures 6a and 6e), but it is accompanied by a strong anticyclone on its east side only for C4 (Figure 6e). Thereafter, both cyclones move southwestward toward the AC. Half a month prior to AC acceleration, as shown in Figures 6b and 6f, the C2 cyclone is completely wrapped into the AC, while the C4 cyclone splits and partly merges into the AC, both molding the meandering path of the AC. Then, both the cyclones experience gradual fusion, contributing to strengthening of the mean flow (Figures 6c and 6g). Afterward, both the AC meanders tended to be advected downstream, with their shape either intact in C4 or dissipated in C2 (Figures 6d and 6h).

The time lag between the AC acceleration and these meanderings may be attributed to the relative positioning of the vortex pair, with the offshore anticyclone migrating slower than the inshore cyclone. This phenomenon is also observed in eddy pairs from the Dutch-South African Agulhas Current sources experiment in May 2008 (de Ruijter et al., 2004), a global data set of automatically tracked eddies (Braby et al., 2016) and Argo in June 2013 (Morris et al., 2019), possibly due to the beta effect during propagation processes (Chelton et al., 2011).

We further discuss the dynamic mechanism governing the cyclone-AC merging process. The diverse trajectories of upstream cyclones (Figure 5b) suggest differences in the timing and location of the merging process for different upstream cyclone events. Therefore, identifying the merging time is essential for conducting a composite analysis subsequently. The merging onset is defined as the moment when a cyclone edge (−0.2 m SLA contours) crosses the eastern boundary of the AC. This boundary is delineated by the eastmost position of the current, where the flow direction matches that of the core at each latitude. Overall, the merging process initiates approximately 1 month before the acceleration peaks.

The composite vertical structures of PV along the zonal sections, which approximately cross the cyclone centers, are shown in Figure 7. The mean PV values are positive, and their maxima are well confined within the upper 50–150 m depth. The climatological PV gradient is significantly strong within 50–100 km offshore (Figure 7a) and acts as an inhibitor of cross-stream mixing (Beal et al., 2006). Upon the onset of merging, there is an anomalous positive PV associated with the cyclone at the eastern boundary of the AC, which substantially diminishes the surrounding PV gradient (Figure 7b). This reduction can be attributed to the negative relative vorticity and the enhanced upper-layer stratification due to the uplifted isopycnals. The composite Hovmöller diagram of PV (Figure 7c) verifies our inference: Before the arrival of cyclones, a substantial zonal PV gradient is observed within approximately 80 km of the coast. Approximately 25 days prior to the merging events, a positive PV signal propagates westward from 400 km offshore. When cyclones collide with the AC (−5 to 5 days), the zonal PV gradient obviously decreases. A weakening of the PV gradient means a reduction in the PV barrier, thus allowing the cyclonic eddies to cross the main current. Thereafter, the AC wraps around the cyclone forming a meander. This merging process occurs at different locations, implying the meanders are not uniquely generated in the Natal Bight. The viewpoint is well-established in the literature (de Ruijter et al., 2004; Elipot & Beal, 2015; Tsugawa & Hasumi, 2010).

For the local cyclone cases, an anticyclone approaches the AC initially (Figure 8a). Approximately 1 month before the acceleration peaks, the anticyclone starts to impinge on the AC (Figure 8b). Approximately 15 days before the peaks, the anticyclone continues to squeeze the AC, which is followed by the emergence of a cyclonic anomaly on the southern inner side of the jet and the meandering ADT contours (Figure 8c). Then, the pair of vortex anomalies propagates downstream. At the peaks of the events, they reach Port Edward, signifying synchronization of the AC acceleration and its meandering (Figure 8d). Thereafter, the cyclone continued propagating downstream, maintaining its shape and strength, while the anticyclone decayed gradually with time and finally dissipated (Figures 8e and 8f).

5. Eddy-Mean Flow Interaction Associated With Energy Anisotropy

To further explore the mechanism governing the generation and development of local cyclones, an eddy-mean flow energy cascade analysis was conducted (Equation 2). Our energy budget analysis highlights the significant role of the barotropic instability process, in agreement with Tsugawa and Hasumi (2010) and Elipot and Beal (2015). During acceleration peaks for the local cyclone cases, KmKe1 displays positive values east of Port
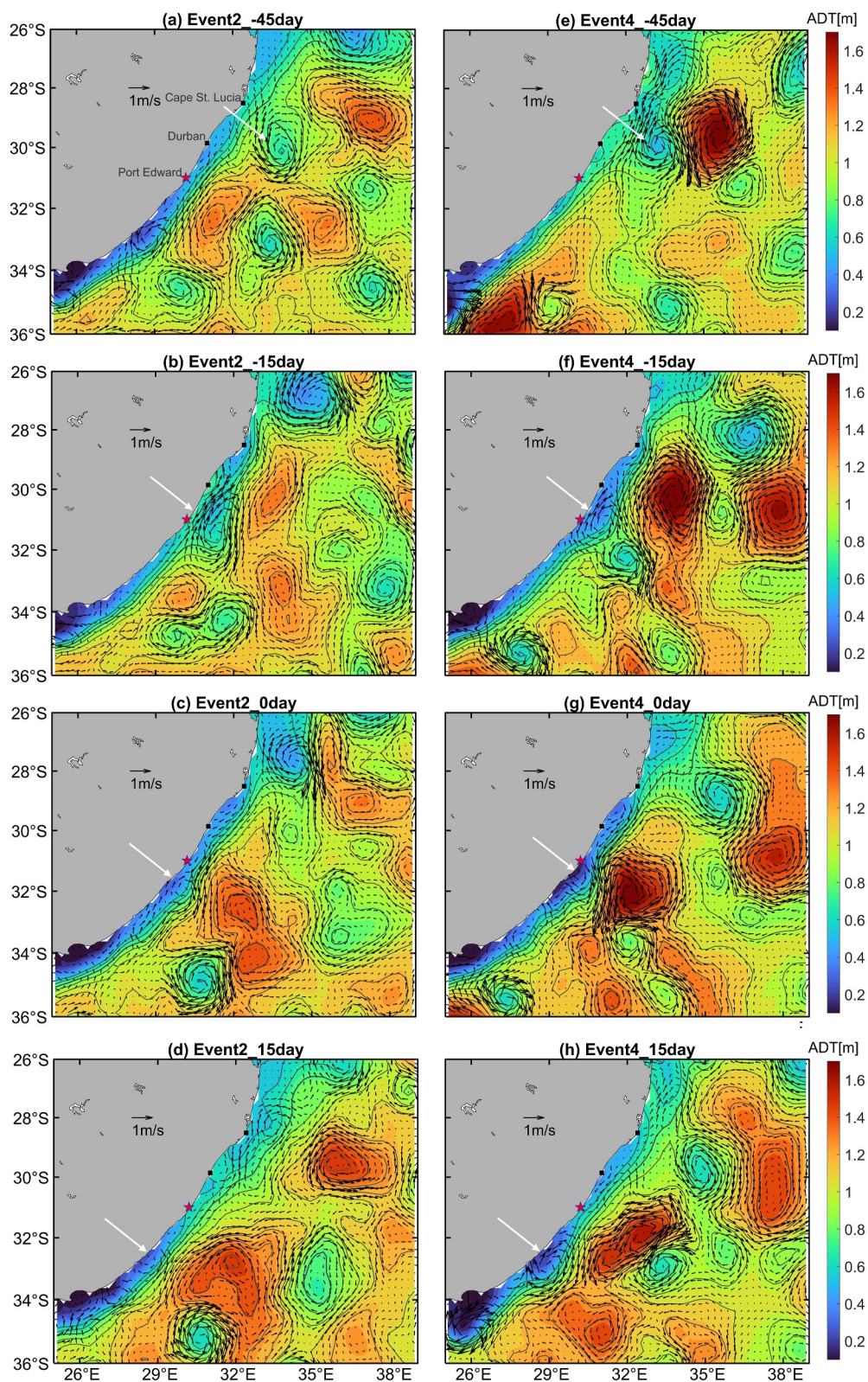
Figure 6. ADT (color shading) and velocity anomalies (vectors) before and after the second (left panels) and fourth (right panels) acceleration event peaks. The gray lines are ADT contours with an interval of 0.1 m. The white arrows indicate the location of the AC meander resulting from the cyclone-AC merging.
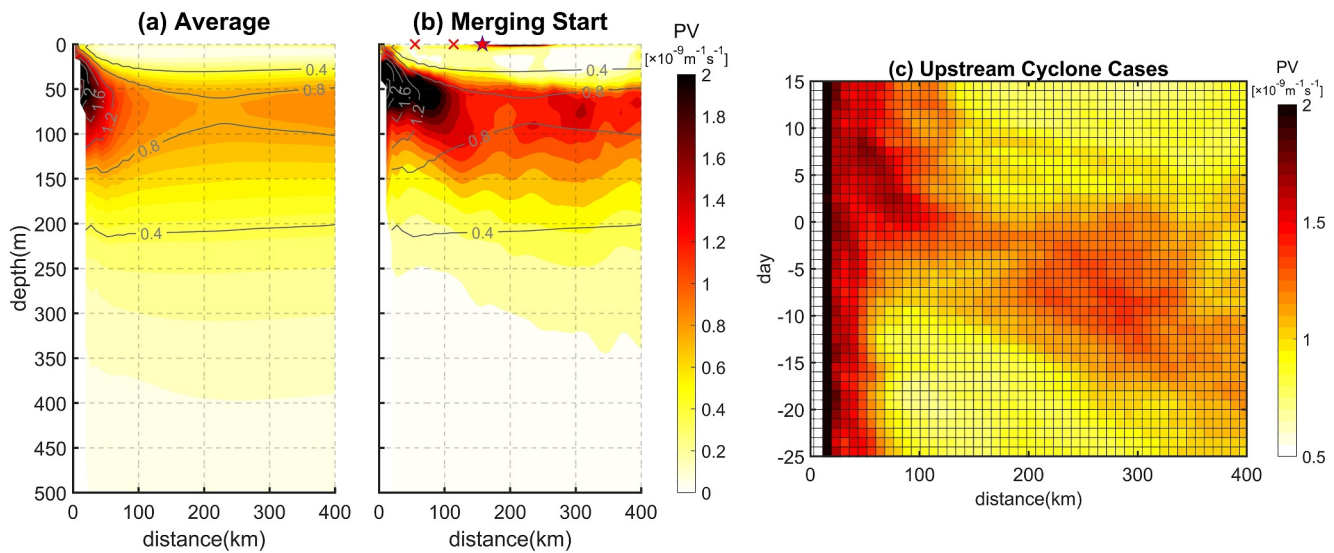
Figure 7. (a) Climatological potential vorticity (PV) along the zonal section. (b) Composited PV for the upstream cyclone cases at the start of cyclone-AC merging. The zonal sections are determined by the locations of cyclones. The gray contours depict the average PV. The pentagram and crosses indicate the mean position of the cyclone centers and AC boundaries, respectively. (c) Hovmöller diagrams of composited PVs for upstream cyclone cases along the zonal section, averaged between 50 and 150 m depth. The horizontal axis represents the distance from the coastline, and the vertical axis represents the days before and after the onset of merging.

Edward (Figure 9a), coinciding with the development of inner-side cyclones (Figure 8d) due to the transfer of kinetic energy from the western boundary current to eddies. Inshore negative KmKe1 values can also be observed, which heralds the local inverse energy cascade from eddies to mean flow and the subsequent decay of meanders in some extent. This inhomogeneous KmKe1 pattern within meanders is also observed in previous studies (Tsugawa & Hasumi, 2010; Yamagami et al., 2019). The maximum KmKe1 at each latitude (Figure 9b) reflects its variability and southward migration. Approximately 20 days before the event, KmKe1 displays weak positive values around the Natal Bight, contributing to the emergence of cyclones (Figures 8b and 8c). Subsequently, the positive KmKe1 signal propagates downstream and gradually intensifies, with the strongest values occurring approximately 10 days before and after the acceleration peaks, sustaining the growth and persistence of the cyclone by the energy cascade from the mean flow. The magnitude of KmKe1 decreases thereafter, corresponding to the slow growth of cyclones (Figure 8e). This further confirms the key role of kinetic energy transfer in the generation and development of cyclones.

Additionally, we calculate the PmPe1 (red contours in Figure 9a). The ratio of KmKe1 to PmPe1 is 1.87 within the eddy-AC interaction region, indicating that barotropic energy transfer is more substantial. Positive values of PmPe1 are predominantly observed within anticyclones for all three groups of acceleration events, consistent with the negative potential density anomalies shown in Figure 2c. This suggests that the potential energy of the AC converts to anticyclones, which is unrelated to the development of cyclonic anomalies. Additionally, high PmPe1 values appear in the inshore region, due to the inclination of the potential density surface probably caused by the offshore excursion of the AC. The positive PmPe1 could be largely counterbalanced by the negative KmKe1, leading to an insignificant effect of eddy-mean flow interaction along the coast.

Based on Equation 6, KmKe1 is further separated into isotropic and anisotropic production components. As shown in Figure 9c, isotropy production is negligible, probably attributed to the relatively small mean divergence within the AC. However, the spatial distribution of the anisotropic production exhibited strong consistency with that of KmKe1 (Figure 9d). Thus, KmKe1 is primarily attributed to its anisotropy production component. The approximation in Equation 9 is reasonable within the AC region.

The anisotropy production is further decomposed according to Equation 9. Eddy anisotropy L (Figure 10a) exhibits high values at the periphery of the eddy-AC interaction region and in the inshore region, indicating the deformation and orientation of eddies. The angle of $\vec{L}$ tends to concentrate at approximately 180° (Figure 10b) within the offshore region (boxes in Figure 10e), indicating that eddy deformation term M is negative and is much stronger than eddy tilting term N. This suggests that the eddies primarily elongate meridionally due to the
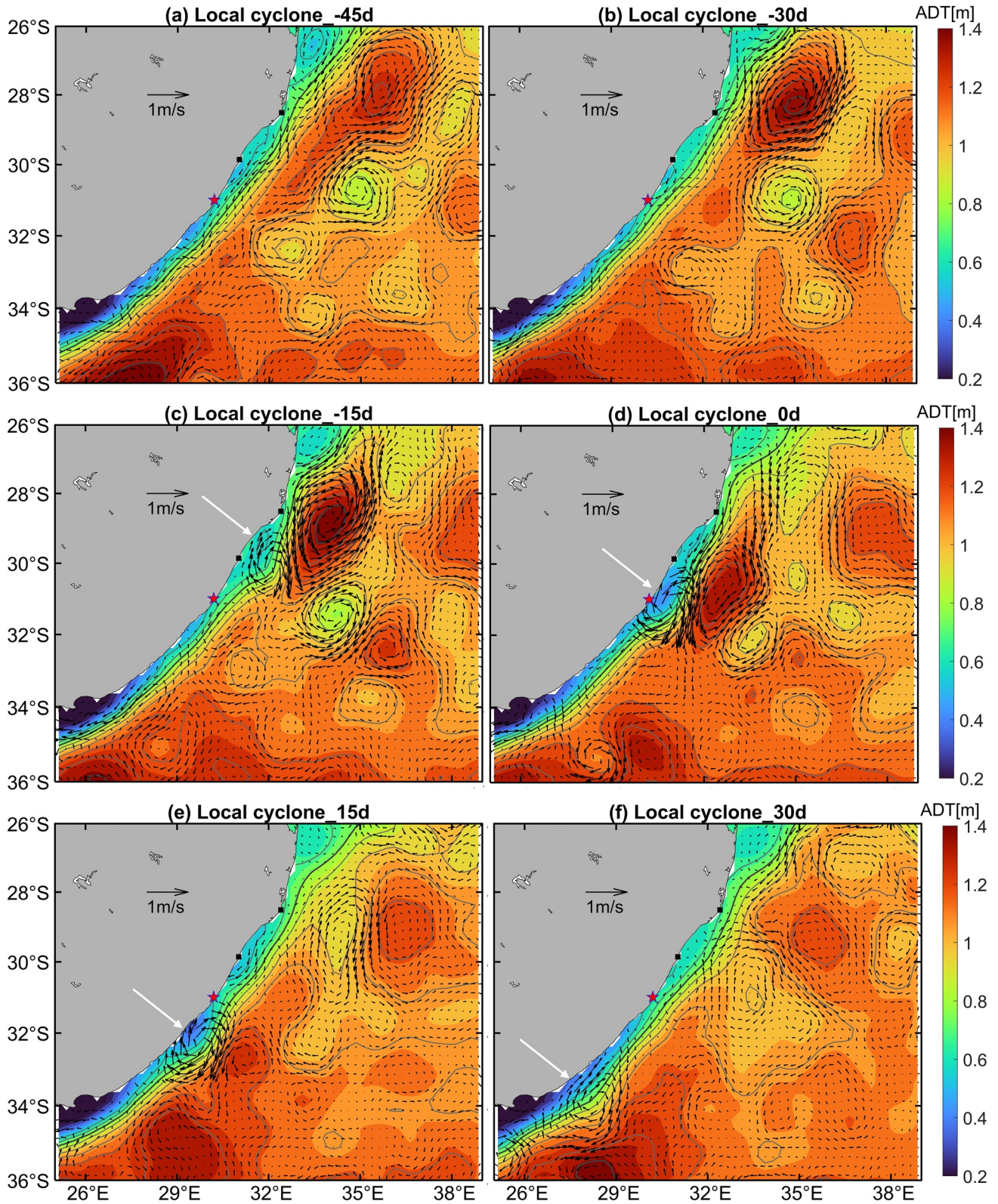
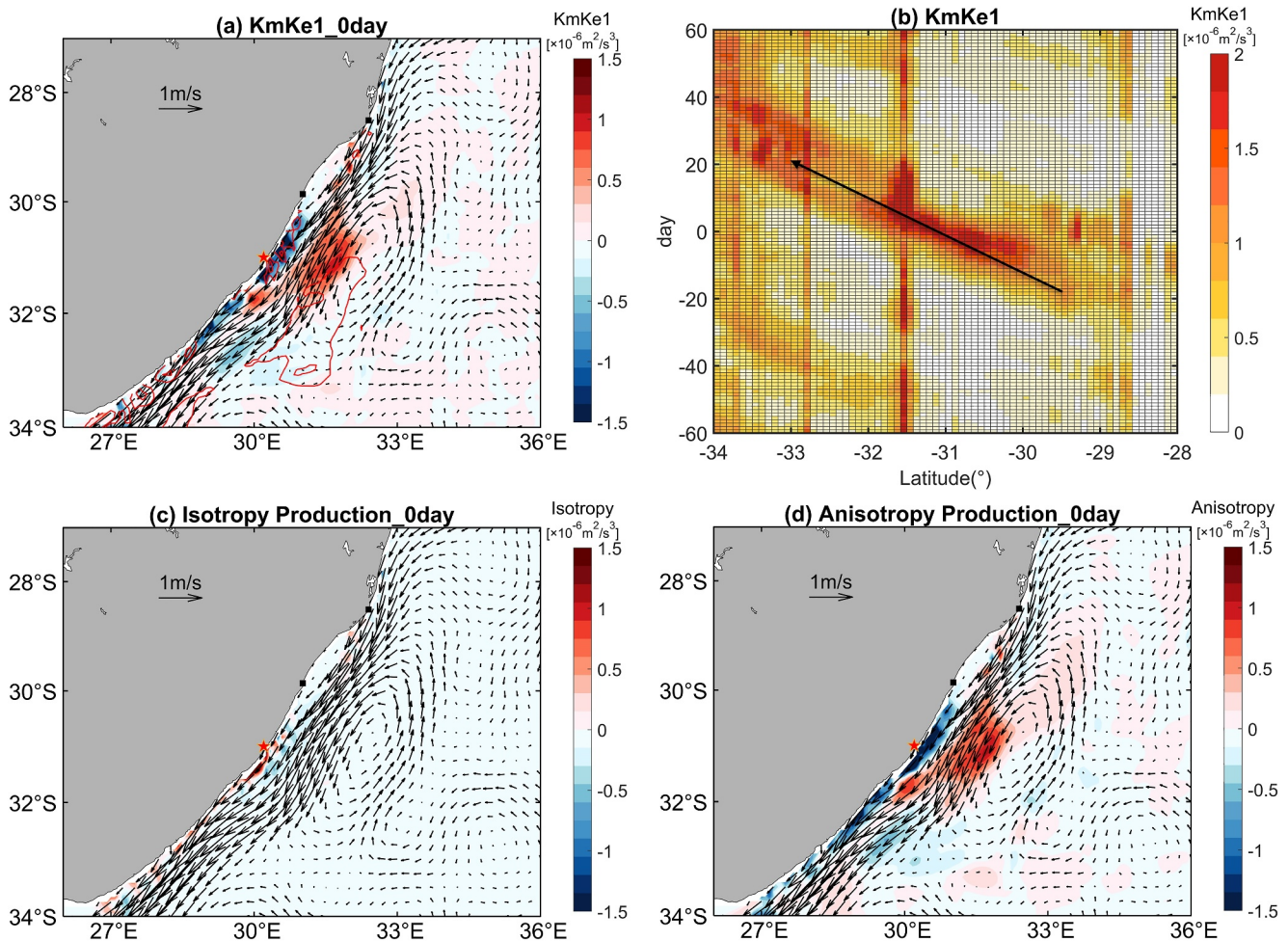**Figure 8.** Same as in Figure 4 but for the composite of local cyclone cases.

Figure 9. (a) Composite of the kinetic energy conversion rate between the AC and eddies (KmKe1, color shadings) and surface geostrophic velocities (vectors) for local cyclone cases averaged in the upper 550 m at the acceleration peaks. The red contours indicate the 0.5 and $1.5 \times 10^{-6} m^2/s^3$ potential energy conversion rate (PmPe1). (b) Composite maximum of KmKe1 at each latitude before and after the acceleration peaks of local cyclone cases. The horizontal axis represents the latitude, and the vertical axis represents the time in days before and after the peaks. (c) and (d) Same as (a), but the isotropy and anisotropy production of KmKe1, respectively.

squeezing effect of AC. Within the inshore region, the concentration of $2\theta_a$ at 120° results from a strong positive N. This indicates a powerful coupling between eastward and northward velocity anomalies caused by coastal cyclonic meanders.

The positive mean flow strain rate (Figure 10c) is evident throughout the entire AC, though it appears to decrease in the eddy-AC interaction region. The negative anomalies will be analyzed in detail later. According to the orientation of $\overrightarrow{S}$ (Figure 10d), positive stretch strain S_n dominates the horizontal strain rate in the offshore region, while negative S_n is also significant in the inshore region. Shear strain S_s exhibits insignificant magnitude. The contrasting spatial pattern of S_n indicates that the mean flow zonally stretches in the offshore flank, while compresses in the inshore flank. These behaviors are attributed to the dynamic structure of the AC with a strong core. Specifically, zonal velocities of the mean flow enhance from its offshore edge toward the strong core, leading to a stretching effect. Contrarily, zonal velocities reduce from the flow core toward the inshore edge, causing a compressing effect.

Due to the meridional elongation of eddies and zonal stretching of the mean flow, the $\overrightarrow{L}$ and $\overrightarrow{S}$ exhibit contrary direction in the interaction region (Figure 10e), facilitating kinetic energy transfer from the mean flow to eddies in Figure 9a. On the contrary, $\overrightarrow{L}$ relatively aligns with $\overrightarrow{S}$ near the coast, leading to a negative cascade. Given the
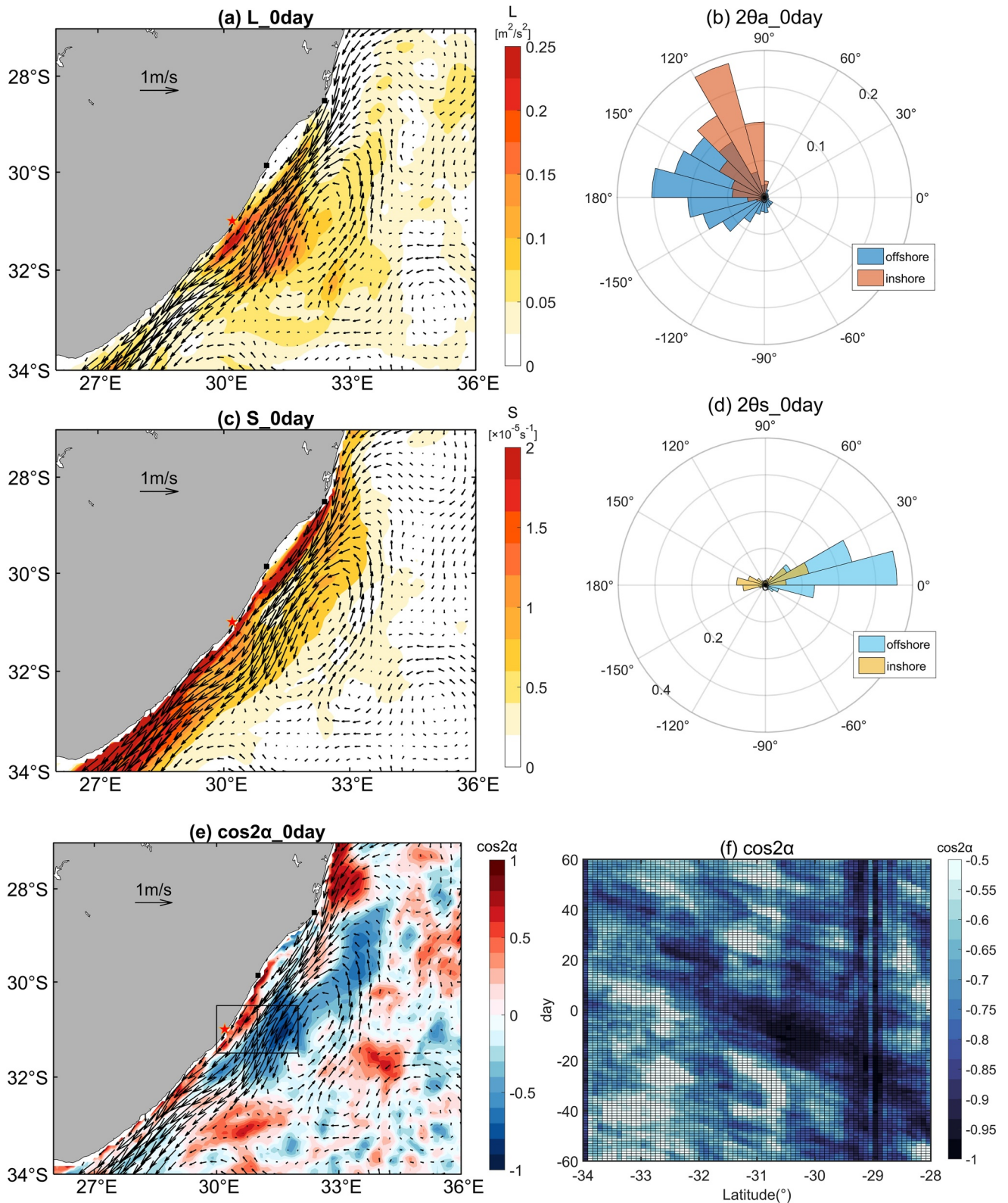
Figure 10. Composite eddy kinetic energy associated with anisotropy L (a), mean flow strain rate S (c), and cosine of orientation parameters 2α (e) for local cyclone cases, averaged over the upper 550 m at the acceleration peaks. Vectors represent composite velocities. Two black boxes highlight the inshore (30–31°E, 30.5–31.5°S) and the offshore (31–32°E, 30.5–31.5°S) regions. Histograms of their orientation parameters $2\theta_a$ (b) and $2\theta_s$ (d) within the offshore and inshore region in the upper 550-m depth at acceleration peaks. Composite minima of $cos\,2\,\alpha$ (f) at each latitude before and after the acceleration peaks of local cyclone cases.
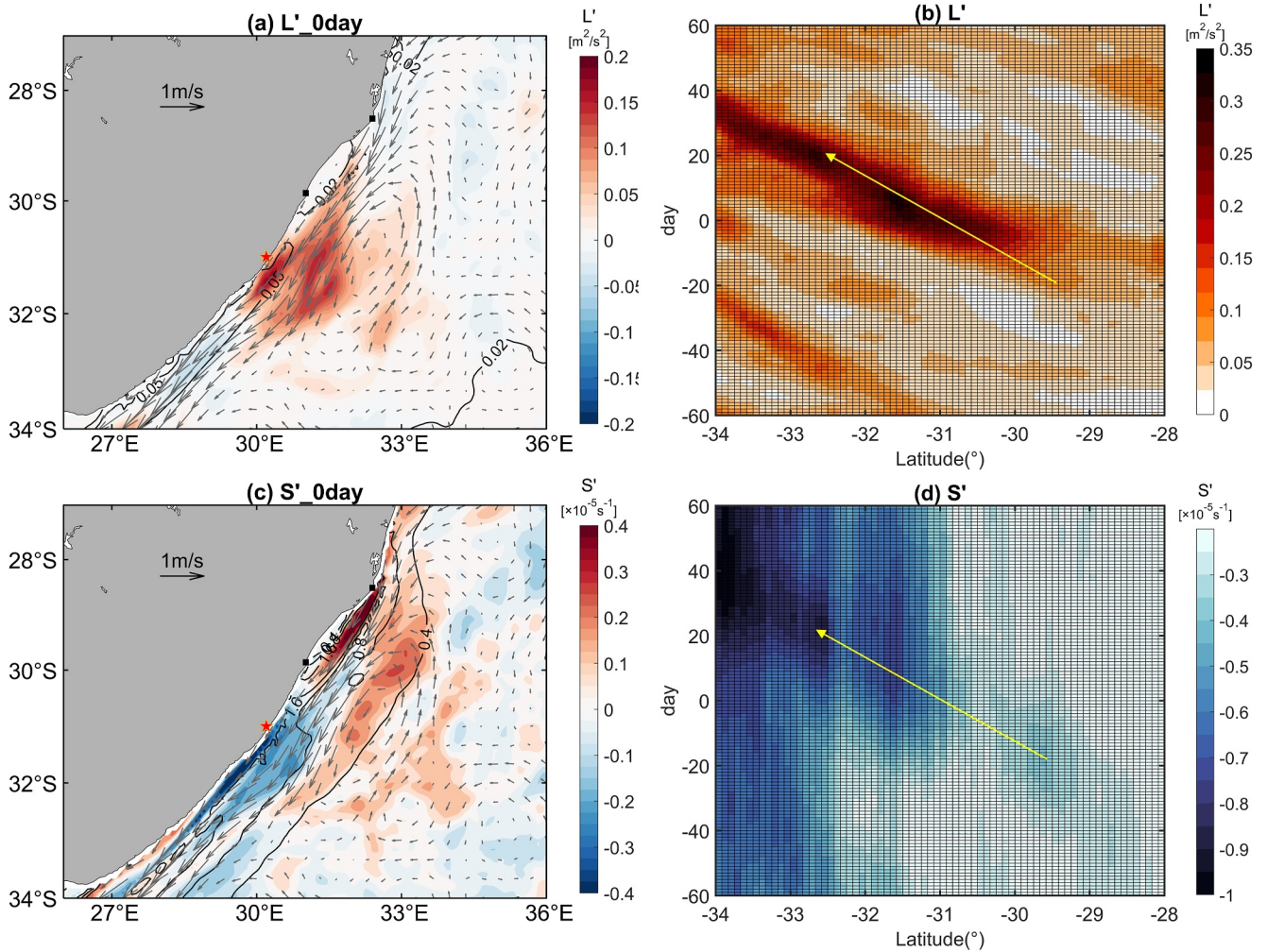
Figure 11. Composite anomalies of L (a) and S (c) for local cyclone cases, averaged over the upper 550 m at the acceleration peaks. Vectors represent composite velocities. The gray lines indicate the averaged L and S contours. Composite maxima of L anomalies (b) and minima of S anomalies (d) at each latitude before and after the acceleration peaks of local cyclone cases.

balance between negative KmKe1 and positive PmPe1 in the inshore region, our next analysis primarily focuses on the offshore eddy-mean flow interaction region.

The variability and migration of cosine values for 2α (Figure 10f) indicates that $\vec{L}$ keeps an opposite direction to $\vec{S}$ from upstream to downstream, promising a positive cascade in the whole eddy-AC interaction process. Based on this downscale energy conversion, the contribution of changes in L and S magnitude to the changes in KmKe1 are evaluated.

High anomalies of KmKe1 or anisotropy production coincide with high anomalies of L at the periphery of the interaction region, implying the deformation and rotation of eddies (Figure 11a). The evolutions of the L anomalies are depicted in Figure 11b. Initially, a weak positive L anomaly is observed around the Natal Bight, promoting a positive energy cascade (Figure 9b) and the development of cyclonic meandering. The subsequent growth of the cyclone and the squeezing of the anticyclone, in turn, further facilitate the increase in along-stream L and positive KmKe1. This process establishes positive feedback, that is, the meanders persistently fuel their growth by enhancing eddy anisotropy.

In Figure 11c, the anomalies of the negative strain rate coincide with the acceleration of the AC. Considering the mean state of the AC structure, that is, a gradual increase in speed from upstream to downstream, the acceleration anomalies associated with the anticyclones could reduce the along-stream velocity gradient and cross-stream

lateral shear. This is in line with classic barotropic instability theory (Sheremet et al., 1995). The effect of the growth of a meander on the reduction in cross-stream shear has also been reported in other studies (Leber & Beal, 2014; McMonigal et al., 2020; van der Vaart & de Ruijter, 2001). Both the AC acceleration and its meandering contribute to the local decrease in stretch and shear strain effects, leading to a reduced KmKe1 and more stable AC, although no alteration in the direction of energy conversion. The minimum strain anomaly at each latitude (Figure 11d) reflects the strengthening and southward migration resulting from enhanced acceleration and meandering. The negative strain anomalies become pronounced approximately 10 days after the acceleration peaks, contributing to the attenuation of KmKe1 (Figure 9b). This process establishes a negative feedback loop, that is, the meanders inhibit their own growth by reducing the mean flow strain rate. The positive effect of the changes in eddy anisotropy and the negative effect of the changes in the AC strain rate work together to influence the development of meandering.

According to previous studies, AC meanders may either grow (de Ruijter et al., 1999; Elipot & Beal, 2015) or dissipate (Rouault & Penven, 2011; van der Vaart & de Ruijter, 2001) downstream. In our observation of 8 local cyclone cases, 5 meanders eventually decay. According to our analysis, the fate of these meanders probably depends on peer competition between the two feedback mechanisms. Once negative feedback dominates, the development of meanders would slow down due to the reduction of the positive energy cascade.

For the upstream cyclone cases, in addition, the energy conversion between cyclones and the AC occurs after their merging, explaining the sustained development of AC meandering. L, S, and 2α (figure not shown) exhibit similar patterns to those of the local cyclone cases but further downstream. For the no cyclone cases, no signals of energy conversion can be detected even though anticyclones are present on the east side of the AC. Statistical results from previous studies also indicate that only a fraction of upstream anticyclones can instigate meanders (Backeberg et al., 2008; Elipot & Beal, 2015; Krug et al., 2014; Krug & Tournadre, 2012). According to our KmKe1 decomposition, the great contrast between the no cyclone and local cyclone cases may lie in the anticyclone-AC colliding position and its alignment with the AC. In the local cyclone cases (Figure 12a), the anticyclones collided with the AC northeast of the Natal Bight. The southwest edge of anticyclones interacts with the fully constituted AC (Beal et al., 2006; Lutjeharms, 2007) and brings relative offshore velocity anomalies, leading to an 2α distribution favoring a positive energy cascade (Figure 12c). This explains the relative southwest position of the cyclonic anomalies in Figure 8c. In addition, the curved coastline of the Natal Bight provides a place for the development of cyclonic anomalies. In the no cyclone cases (Figure 12b), some anticyclones perform as ellipses aligning with the AC, and some anticyclones laterally collide with the AC south of the Natal Bight, bringing relative along-stream velocity anomalies. For the stretch-dominant background flow, both of these situations lead to a relative orientation between $\overrightarrow{L}$ and $\overrightarrow{S}$ of approximately 90° (Figure 12d). This impedes energy conversion, resulting in the absence of meandering. In conclusion, the tracks and orientations of anticyclones before they collide with the AC could determine whether meandering develops. The reduced-gravity model also emphasizes whether eddies gain kinetic energy from the mean flow is mainly determined by their orientations (Kuo & Chern, 2011), which aligns with our results to some extent.

6. The Generation of AC Meandering During Nonacceleration

We have analyzed the origin of meanders in the presence of AC acceleration, but can meanders form without the AC acceleration? The 10-day moving average longitudinal position of the AC core at Port Edward is examined. Meanders are defined as offshore displacement of the AC core exceeding 2 std (approximately 50 km) from the mean (Figure 13a). The selection of the 10-day moving window is based on the average timescale of 10.2 days associated with alongshore fluctuations (Bryden et al., 2005) and the 10-day filtering cutoff for identifying meanders (Rouault & Penven, 2011). A total of 53 meander events are identified from January 1993 to June 2020, averaging about 1.92 events per year, which is close to 1.8 per year (Yamagami et al., 2019) and two per year (Rouault & Penven, 2011). Most meanders are associated with acceleration (16 cases stronger than one std), far less are associated with deceleration (4 cases weaker than one std). This implies that AC tends to accelerate rather than decelerate. 20 meanders without acceleration are picked out based on the criterion that the core intensity is weaker than its climatological average. The composite of these 20 nonaccelerating meanders (Figure 13c) shows a meandering path of the AC with an intact anomalous cyclonic circulation and strong negative SLA, paralleled with weaker positive SLA offshore. This pattern differs from that of the acceleration events with local cyclone
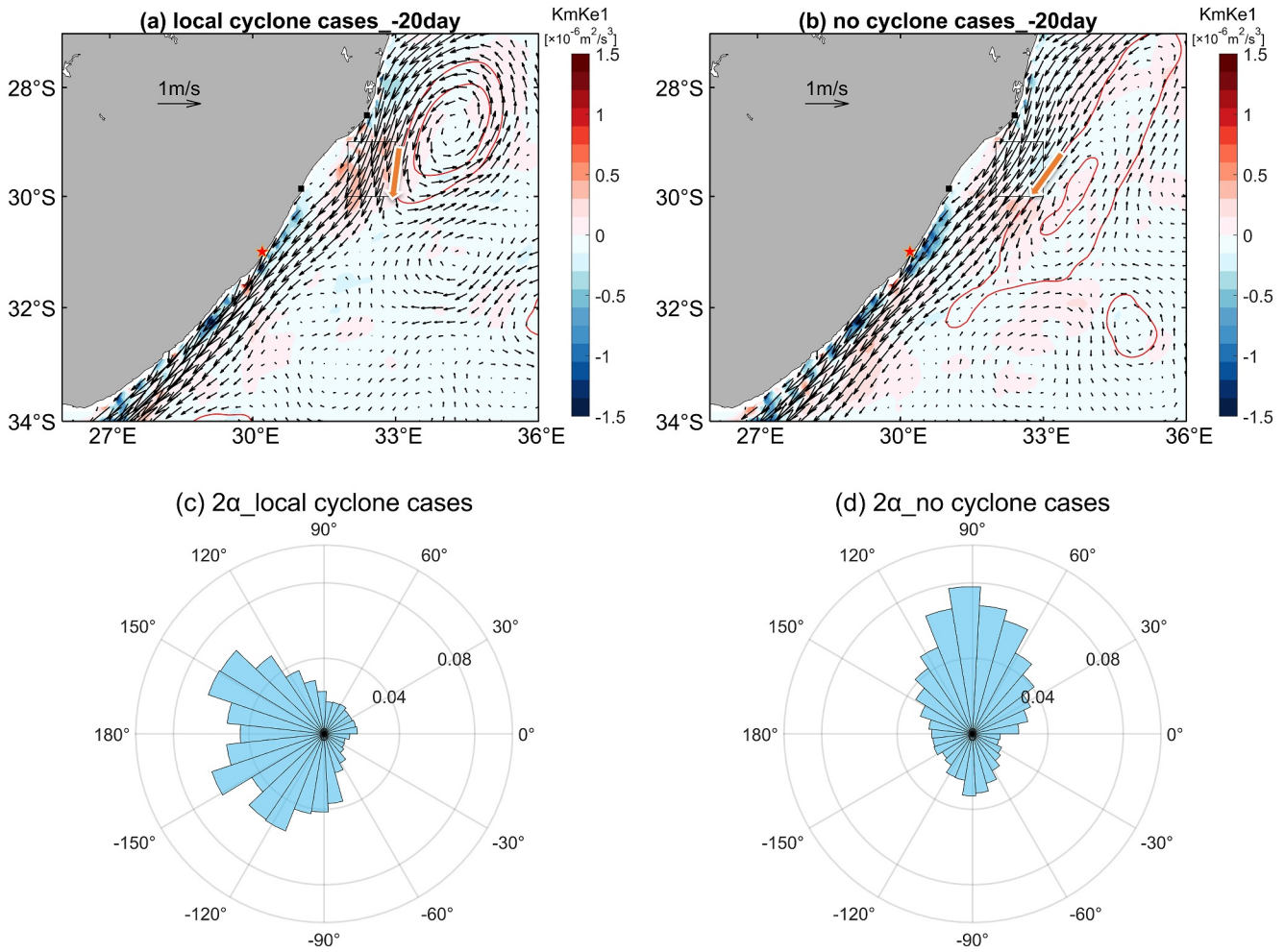
Figure 12. Composite of KmKe1 for local cyclone cases (a) and no cyclone cases (b), averaged in the upper 550 m at 20 days before the acceleration peaks. The vectors represent composite velocities, and the red lines are the 0.8 and 0.9 m reanalysis SSH contours. The arrows indicate the direction of velocity anomalies due to the eddies. Histograms of orientation parameters 2α for local cyclone cases (c) and no cyclone cases (d) in the upper 550 m depth at −20 days relative to the acceleration peaks. The statistical region is highlighted in Figure 11a.

cases in Figure 5d. The intensity of the AC core is weakest (0.71 m/s) approximately 5 days before the meandering peaks, implying a deceleration effect induced by cyclonic eddies before crossing the current.

Positive EKE anomalies (Figure 14a) are observed in the upstream regions before the AC nonacceleration meanders, particularly in the area at 27°S which has detached from the AC. To observe the propagations of negative SLA signals resulting from the divergence of cyclonic eddies, AC, MC, and south of Madagascar sections were established. In Figure 14b, negative SLA signals can be traced back to the upstream regions (marked by arrows), indicating that the cyclonic anomalies probably form at Delagoa Bay or south of Madagascar, aligning with the upstream cyclone cases of acceleration events in Figure 5b. The propagation speed is steady at 9.1 km/d, aligning with the EKE anomalies and the average speed of 4.3–11 km/d in previous studies (de Ruijter et al., 2004; Morris et al., 2019).

The composite Hovmöller diagram of PV (Figure 14c) resembles that of acceleration events with cyclones from upstream (Figure 7c). These nonlocal cyclones reduce the PV gradient barrier within the AC, facilitating their entry into the main current. Unlike the acceleration events with locally formed cyclones (Figure 9a), KmKe1 (Figure 14d) does not exhibit significant positive values, indicating that the process of anticyclones triggering downscale kinetic energy conversion scarcely contributes to the generation of these nonaccelerating meanders. We further visually examined the source of 20 nonaccelerating meander events one by one. Among them, cyclonic anomalies in 17 events originated from upstream regions and merged with the AC, while the remaining 3
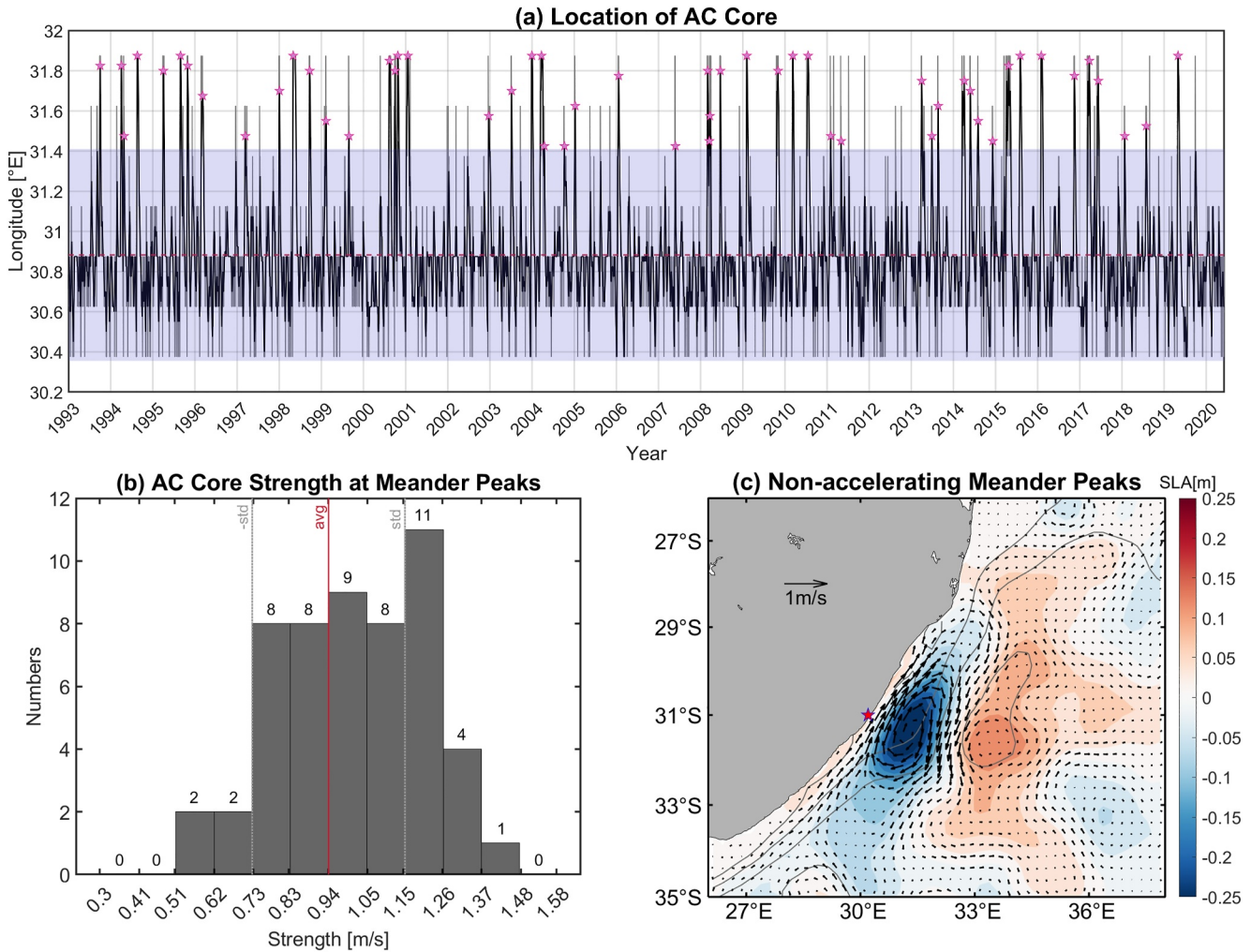
Figure 13. (a) Time series of the AC core location at 31°S. The black (gray) series represents the location after (before) applying a 10-day moving average. The red dashed line and the purple shadow denote the mean and ±2std, respectively. The pink pentagrams designate the peaks of each meander event. (b) Histogram of 10-day moving average AC core strength at meander peaks. The vertical lines denote the climatological mean and standard deviation of 10-day moving average AC core strength. (c) Composites of the SLA and geostrophic flow anomalies during 20 nonaccelerating meander peaks. The gray contours represent the ADT.

events were generated locally accompanied by anticyclones offshore. A natural question is why the AC did not accelerate with anticyclone facilitation for these three events. Actually, the AC core accelerates approximately 5 days after the meander peaks, rather than precisely at the peaks.

Meanders with and without acceleration suggest that three distinct eddy-mean flow interaction processes contribute to meander generation associated with different variabilities in the intensity of the AC core. First, single cyclones from upstream cross or partially cross the AC, inducing meandering flows. The AC core would not be strengthened, and sometimes even weakened, because the current bypasses the cyclones. Second, single anticyclones from upstream accelerate the AC. Some anticyclones encounter the AC with nonparallel orientations, favoring downscale kinetic energy transfer and then promoting meander formation. Third, dipole eddies interact with the AC. Merging cyclones shift the AC offshore while anticyclones strengthen the current.

7. Conclusions and Discussion

Rhythms of the Agulhas Current, that is, its acceleration and meandering, are investigated on the basis of satellite altimetry data and high-resolution GLORYS reanalysis products from 1993 to 2020, with a focus on the effect of energetic anisotropy on the generation of meanders. The results suggest that eddy-mean flow interaction plays a key role in the spatial and temporal variations of the AC, involving three different types of eddies: single
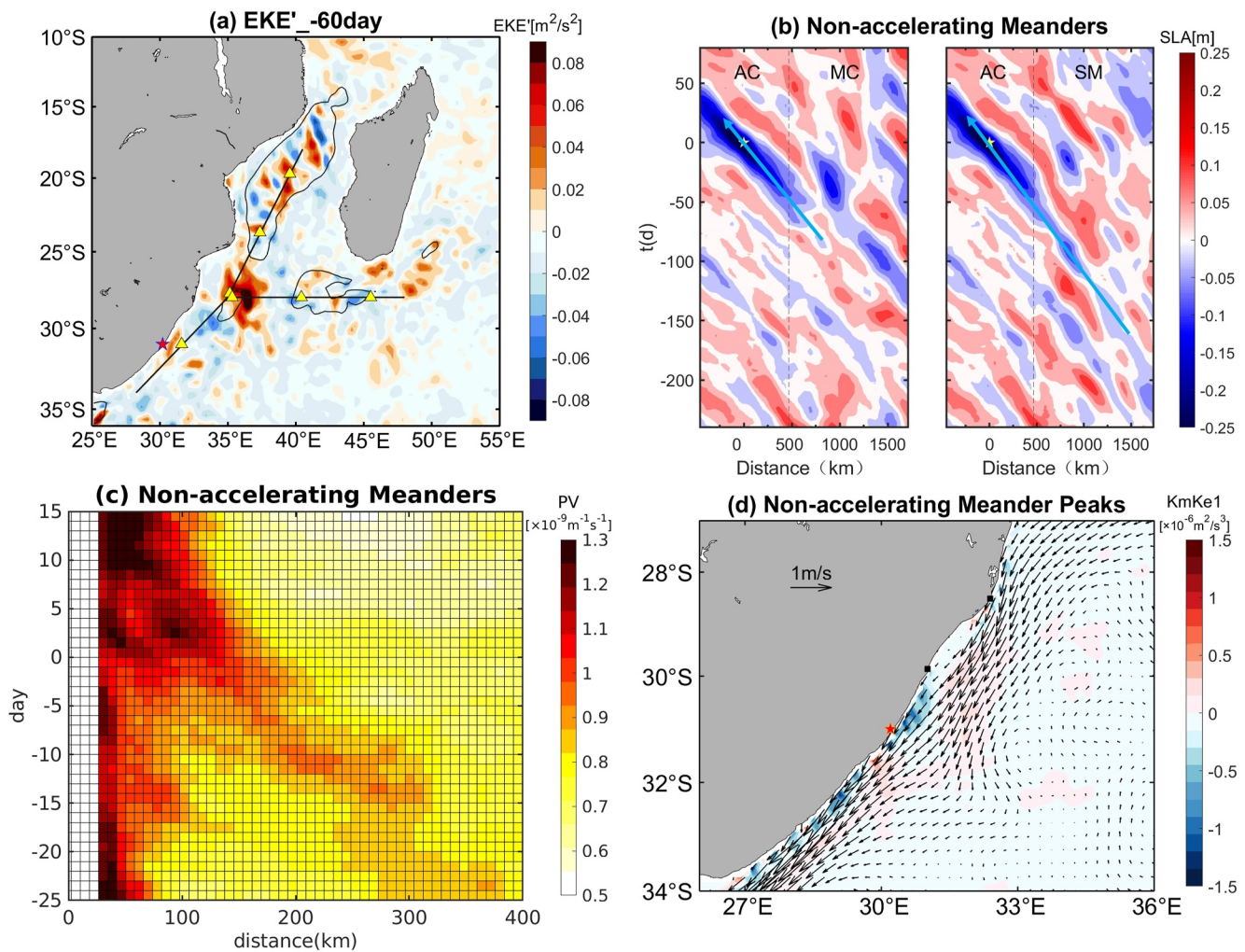
Figure 14. (a) Composite EKE anomalies 60 days before the nonaccelerating meander peaks. The thin black contours enclose the regions with climatological EKE values exceeding 0.09 m²/s². The thick black lines and yellow triangles denote the section for the SLA Hovmöller diagrams and indicate distance intervals of 500 km in Figure 15b. (b) Composite Hovmöller diagrams of SLA along the MC-AC section (left panel) and SM-AC section (right panel). The horizontal axis represents the distance to the AC section at 31°S (positive values indicate the upstream direction), and the vertical axis represents the days before and after the nonaccelerating meander peaks. Dashed vertical lines and pentagrams denote the junctions of the two sections and the peaks of meanders, respectively. (c) Hovmöller diagrams of composited PVs for nonaccelerating meander peaks along the 31°S zonal section, averaged between 50 and 150 m depth. The horizontal axis represents the distance from the coastline, and the vertical axis represents the days before and after the peaks. (d) Composite of KmKe1 for nonaccelerating meander peaks, averaged in the upper 550 m. The vectors represent composite velocities.

anticyclones, single cyclones, and paired antipolar eddies. The composite analyses show that the single anticyclones originating from the Mozambique Channel and East Madagascar Current lead to a significant increase in AC velocity and a seesaw-like vertical displacement of isopycnals. During the process of squeezing and entrainment, the anticyclones rotate and elongate into ellipses aligned parallel to the AC (Figure 15a).

The AC meanders without acceleration are linked to the influence of single cyclones. These upstream cyclones reduce the potential vorticity barrier of the AC, facilitating their merger into the current. To envelop these cyclones, the AC meanders along a pulse-like path. In contrast, the meandering behavior during acceleration events can arise from two different physical processes. The first one involves the interaction between the AC and paired vortices emanating from the EMC, where anticyclones accelerate the AC and cyclones crossing the current cause it to meander. The second process is associated with local barotropic instability, driven by single anticyclones, which triggers a downscale energy cascade from the AC to perturbations. This finding is essentially consistent with previous studies (de Ruijter et al., 1999; Elipot & Beal, 2015; Schouten et al., 2002; Tsugawa & Hasumi, 2010; Yamagami et al., 2019).
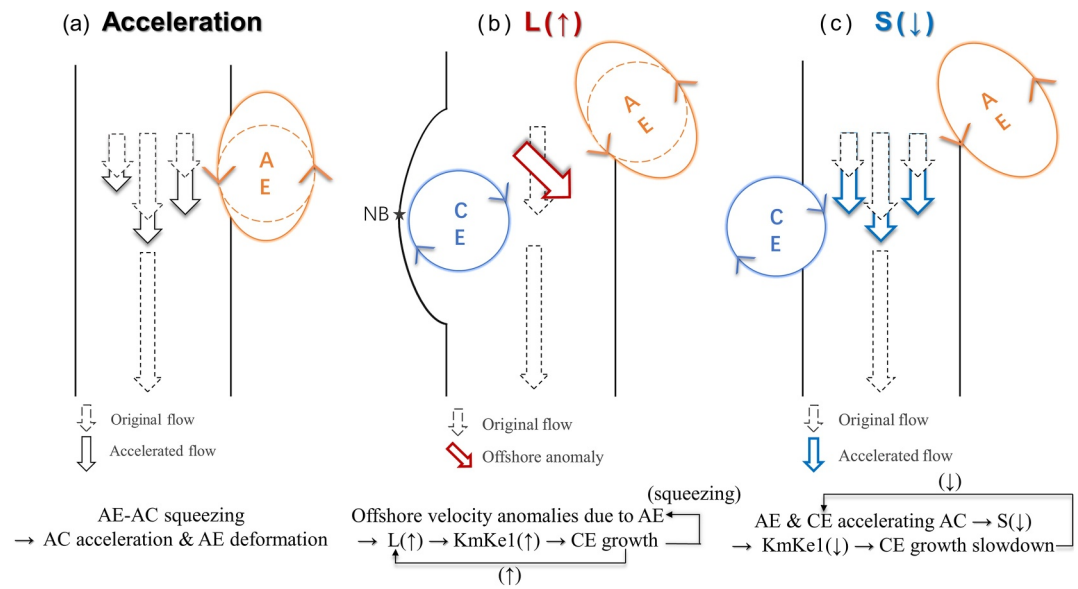
Figure 15. Schematic diagram illustrating the processes of acceleration (a), positive feedback of eddy anisotropy (b), and negative feedback of the mean flow strain rate(c). L, S, and KmKe1 characterize the portion of the eddy kinetic energy associated with anisotropy, the mean flow strain, and the kinetic energy conversion rate, respectively. AE, CE, AC, and NB denote anticyclonic, cyclonic eddy, the Agulhas Current, and the Natal Bight, respectively.

For the first time, we provide additional insights into the variations and feedback mechanisms of eddies and mean flow from the perspective of anisotropic energy decomposition. The results revealed that the development of AC meandering is determined by two feedback mechanisms: the positive feedback of eddy anisotropy and the negative feedback of the accelerated AC strain rate. On one hand, velocity anomalies of anticyclones lead to anisotropic eddy kinetic energy and influence the relative direction between eddy anisotropy and mean flow strain, initiating a downscale energy cascade. As cyclonic anomalies grow and squeeze anticyclones into ellipses, the anisotropic eddy kinetic energy L increases, which further prompts energy conversion (Figure 15b). Therefore, positive feedback is established to foster the development of meanders. On the other hand, the acceleration of the AC caused by mesoscale anomalies exerts a weakening effect on energy conversion by relaxing the strain rate S (Figure 15c), especially the normal strain. This reduction in positive energy cascade inhibits the development of meanders.

Our analysis clarifies the relationship between the acceleration and meanders of the AC. Meanders do not necessarily correspond to the acceleration of the current; rather, the type of eddies interacting with the AC determines its velocity structure. A previous study suggested that barotropic instability may originate from its modulation of flow speed (de Ruijter et al., 1999). In our study, however, the acceleration induced by mesoscale eddies appears to reduce the AC strain. This strain reduction impedes the downscale energy conversion as indicated by anisotropic energy analysis, thereby inhibiting meander development. Previous research has shown that the meandering AC exhibits weaker velocities and a broader structure at nominally 34°S, based on both satellite altimetry (Beal & Elipot, 2016) and moored array data sets (Beal et al., 2015; McMonigal et al., 2020). This implies reduced cross-stream shear (Leber & Beal, 2014) and strain, limiting the growth of the meander (van der Vaart & de Ruijter, 2001), which aligns with our results to some extent.

Recent studies indicate that global oceanic eddies typically have an elliptical (Chen et al., 2019; Wang et al., 2023), or even egg-like shape (Chen et al., 2021), rather than being circular. Our energetic anisotropy analysis suggests that the shape and orientation of anticyclonic eddies influence the direction of energy transfer and the formation of meanders. Studying interactions between elliptical eddies with various flattenings and orientations and western boundary currents could further deepen our understanding of multiscale dynamics.

In addition to the barotropic instability associated with anticyclones, our findings reveal that the direct merging of offshore cyclonic eddies into the AC also displaces the current offshore. Model results suggest that strength of eddies (Sheu et al., 2010), the current's transport strength and that of its curvature (Vandermeirsch et al., 2003),

may dictate if crossing occurs, but how these mechanisms work in the Agulhas system needs further investigation. Parameters such as the relative size, slanting angle (Yan et al., 2016), and colliding position of eddy pairs likely result in a more complex interaction process, influencing both the strength and the path of the current.

Mesoscale eddy activity in the Agulhas system intensified from 1993 to 2009, particularly in the Mozambique Channel and south of Madagascar (Backeberg et al., 2012). Our analysis suggests that the enhancement of the upstream eddy leads to more active eddy-AC interaction, which likely contributes to the rise in both AC acceleration events and meandering events. The frequency of acceleration events has increased (Figure 1b), and more meanders have been observed at 34°S from 1993 to 2015 (Beal & Elipot, 2016; Elipot & Beal, 2015). In future studies, the evolution of these eddies and their specific impacts on the AC acceleration or meandering should be the focus.

Our analysis suggests that eddy anisotropy and the mean flow strain rate counterbalance each other to determine the growth of meanders. Decayed meanders exhibit weaker eddy anisotropy and a stronger mean flow strain rate compared to fully developed meanders, such as those observed in January 2006 and March 2010 (not shown). The distinct development of these two meanders was also identified by the position of the AC at different latitudes, as reported by Rouault and Penven (2011). These two feedback mechanisms influencing meander growth provide a theoretical reference for simulating and forecasting meanders in model studies and have general applicability to other eddy-mean flow interaction regions. For example, similar meandering behaviors triggered by anticyclonic eddies have been studied in the Kuroshio east of Taiwan (Chang et al., 2018; Zhang et al., 2001) and southeast of Kyushu (Ebuchi & Hanawa, 2003; Mitsudera et al., 2001; Miyazawa et al., 2004; Waseda et al., 2002, 2003). In these regions, barotropic instability has been documented to play an important role in the eddy-mean flow interaction processes (Yan et al., 2022; Yang & Liang, 2019). Further energy conversion decomposition within the framework of energetic anisotropy, as used in this study, can provide deeper insights into the feedback of eddy anisotropy and the mean flow strain on the growth of meanders.

Data Availability Statement

All data used in this study are publicly available. The altimetry data set was distributed by the Copernicus Climate Change Service and is available via https://doi.org/10.24381/cds.4c328c78 (Copernicus Climate Change Service & Climate Data Store, 2018). The GLORYS12V1 product identifier is GLOBAL_MULTIYEAR_PHY_001_030 and is available via https://doi.org/10.48670/moi-00021 (Fernandez & Lellouche, 2018). The MATLAB scripts used for data analysis in this study are published on Zenodo at https://doi.org/10.5281/zenodo.13839074 (Guo, 2024).

References

Adeagbo, O. S., Du, Y., Wang, T., & Wang, M. (2022). Eddy–mean flow interactions in the Agulhas leakage region. *Journal of Oceanography*, *78*(3), 151–161. https://doi.org/10.1007/s10872-022-00637-6

Backeberg, B. C., Johannessen, J. A., Bertino, L., & Reason, C. J. (2008). The greater Agulhas Current system: An integrated study of its mesoscale variability. *Journal of Operational Oceanography*, *1*(1), 29–44. https://doi.org/10.1080/1755876X.2008.11020093

Backeberg, B. C., Penven, P., & Rouault, M. (2012). Impact of intensified Indian Ocean winds on mesoscale variability in the Agulhas system. *Nature Climate Change*, *2*(8), 608–612. https://doi.org/10.1038/nclimate1587

Beal, L. M., & Bryden, H. L. (1999). The velocity and vorticity structure of the Agulhas Current at 32°S. *Journal of Geophysical Research*, *104*(C3), 5151–5176. https://doi.org/10.1029/1998JC900056

Beal, L. M., Chereskin, T. K., Lenn, Y. D., & Elipot, S. (2006). The sources and mixing characteristics of the Agulhas current. *Journal of Physical Oceanography*, *36*(11), 2060–2074. https://doi.org/10.1175/JPO2964.1

Beal, L. M., de Ruijter, W. P. M., Biastoch, A., Zahn, R., Cronin, M., Hermes, J., et al. (2011). On the role of the Agulhas system in ocean circulation and climate. *Nature*, *472*(7344), 429–436. https://doi.org/10.1038/nature09983

Beal, L. M., & Elipot, S. (2016). Broadening not strengthening of the Agulhas Current since the early 1990s. *Nature*, *540*(7634), 570–573. https://doi.org/10.1038/nature19853

Beal, L. M., Elipot, S., Houk, A., & Leber, G. M. (2015). Capturing the transport variability of a western boundary jet: Results from the Agulhas current time-series experiment (ACT). *Journal of Physical Oceanography*, *45*(5), 1302–1324. https://doi.org/10.1175/JPO-D-14-0119.1

Biastoch, A., Beal, L. M., Lutjeharms, J. R. E., & Casal, T. G. D. (2009). Variability and Coherence of the Agulhas undercurrent in a high-resolution ocean general circulation model. *Journal of Physical Oceanography*, *39*(10), 2417–2435. https://doi.org/10.1175/2009JPO4184.1

Biastoch, A., Lutjeharms, J. R. E., Böning, C. W., & Scheinert, M. (2008). Mesoscale perturbations control inter-ocean exchange south of Africa. *Geophysical Research Letters*, *35*(20), L20602. https://doi.org/10.1029/2008GL035132

Braby, L., Backeberg, B. C., Ansorge, I., Roberts, M. J., Krug, M., & Reason, C. J. C. (2016). Observed eddy dissipation in the Agulhas current. *Geophysical Research Letters*, *43*(15), 8143–8150. https://doi.org/10.1002/2016GL069480

Bryden, H. L., & Beal, L. M. (2001). Role of the Agulhas Current in Indian Ocean circulation and associated heat and freshwater fluxes. *Deep Sea Research Part I: Oceanographic Research Papers*, *48*(8), 1821–1845. https://doi.org/10.1016/S0967-0637(00)00111-4

Bryden, H. L., Beal, L. M., & Duncan, L. M. (2005). Structure and transport of the Agulhas current and its temporal variability. *Journal of Oceanography*, *61*(3), 479–492. https://doi.org/10.1007/s10872-005-0057-8

Casal, T. G. D., Beal, L. M., Lumpkin, R., & Johns, W. E. (2009). Structure and downstream evolution of the Agulhas Current system during a quasi-synoptic survey in February–March 2003. *Journal of Geophysical Research*, *114*(C3), C03001. https://doi.org/10.1029/2008JC004954

Chang, M.-H., Jan, S., Mensah, V., Andres, M., Rainville, L., Yang, Y. J., & Cheng, Y.-H. (2018). Zonal migration and transport variations of the Kuroshio east of Taiwan induced by eddy impingements. *Deep Sea Research Part I: Oceanographic Research Papers*, *131*, 1–15. https://doi.org/10.1016/j.dsr.2017.11.006

Chelton, D. B., Schlax, M. G., & Samelson, R. M. (2011). Global observations of nonlinear mesoscale eddies. *Progress in Oceanography*, *91*(2), 167–216. https://doi.org/10.1016/j.pocean.2011.01.002

Chen, G., Han, G., & Yang, X. (2019). On the intrinsic shape of oceanic eddies derived from satellite altimetry. *Remote Sensing of Environment*, *228*, 75–89. https://doi.org/10.1016/j.rse.2019.04.011

Chen, G., Yang, J., & Han, G. (2021). Eddy morphology: Egg-like shape, overall spinning, and oceanographic implications. *Remote Sensing of Environment*, *257*, 112348. https://doi.org/10.1016/j.rse.2021.112348

Copernicus Climate Change Service Data Store Climate. (2018). Sea level gridded data from satellite observations for the global ocean from 1993 to present [Dataset]. *Copernicus Climate Change Service (C3S) Climate Data Store (CDS)*. https://doi.org/10.24381/cds.4c328c78

Cossa, O., Pous, S., Penven, P., Capet, X., & Reason, C. J. C. (2016). Modelling cyclonic eddies in the Delagoa Bight region. *Continental Shelf Research*, *119*, 14–29. https://doi.org/10.1016/j.csr.2016.03.006

de Ruijter, W. P. M., van Aken, H. M., Beier, E. J., Lutjeharms, J. R. E., Matano, R. P., & Schouten, M. W. (2004). Eddies and dipoles around south Madagascar: Formation, pathways and large-scale impact. *Deep Sea Research Part I: Oceanographic Research Papers*, *51*(3), 383–400. https://doi.org/10.1016/j.dsr.2003.10.011

de Ruijter, W. P. M., van Leeuwen, P. J., & Lutjeharms, J. R. E. (1999). Generation and evolution of natal pulses: Solitary meanders in the Agulhas current. *Journal of Physical Oceanography*, *29*(12), 3043–3055. https://doi.org/10.1175/1520-0485(1999)029<3043:GAEONP>2.0.CO;2

Ebuchi, N., & Hanawa, K. (2003). Influence of mesoscale eddies on variations of the Kuroshio path south of Japan. *Journal of Oceanography*, *59*(1), 25–36. https://doi.org/10.1023/A:1022856122033

Elipot, S., & Beal, L. M. (2015). Characteristics, energetics, and origins of Agulhas current meanders and their limited influence on ring shedding. *Journal of Physical Oceanography*, *45*(9), 2294–2314. https://doi.org/10.1175/JPO-D-14-0254.1

Fernandez, E., & Lellouche, J. M. (2018). Global Ocean physics reanalysis (issue: 1.1) [Dataset]. *E.U. Copernicus Marine Service Information (CMEMS). Marine Data Store (MDS)*. https://doi.org/10.48670/moi-00021

Gordon, A. L. (1986). Interocean exchange of thermocline water. *Journal of Geophysical Research*, *91*(C4), 5037–5046. https://doi.org/10.1029/JC091iC04p05037

Gründlingh, M. L. (1983). On the course of the Agulhas current. *South African Geographical Journal*, *65*(1), 49–57. https://doi.org/10.1080/03736245.1983.10559671

Gula, J., Molemaker, M. J., & McWilliams, J. C. (2014). Submesoscale cold filaments in the Gulf stream. *Journal of Physical Oceanography*, *44*(10), 2617–2643. https://doi.org/10.1175/JPO-D-14-0029.1

Guo, X. (2024). MATLAB scripts for analysing data in paper Rhythms of the Agulhas current within the framework of energetic anisotropy (version v3) [Software]. *Zenodo*. https://doi.org/10.5281/zenodo.13839074

Krug, M., & Tournadre, J. (2012). Satellite observations of an annual cycle in the Agulhas Current. *Geophysical Research Letters*, *39*(15). https://doi.org/10.1029/2012GL052335

Krug, M., Tournadre, J., & Dufois, F. (2014). Interactions between the Agulhas current and the eastern margin of the Agulhas bank. *Continental Shelf Research*, *81*, 67–79. https://doi.org/10.1016/j.csr.2014.02.020

Kuo, Y.-C., & Chern, C.-S. (2011). Numerical study on the interactions between a mesoscale eddy and a western boundary current. *Journal of Oceanography*, *67*(3), 263–272. https://doi.org/10.1007/s10872-011-0026-3

Leber, G. M., & Beal, L. M. (2014). Evidence that Agulhas Current transport is maintained during a meander. *Journal of Geophysical Research: Oceans*, *119*(6), 3806–3817. https://doi.org/10.1002/2014JC009802

Leber, G. M., & Beal, L. M. (2015). Local water mass modifications by a solitary meander in the Agulhas Current. *Journal of Geophysical Research: Oceans*, *120*(6), 4503–4515. https://doi.org/10.1002/2015JC010863

Leber, G. M., Beal, L. M., & Elipot, S. (2017). Wind and current forcing combine to drive strong upwelling in the Agulhas current. *Journal of Physical Oceanography*, *47*(1), 123–134. https://doi.org/10.1175/JPO-D-16-0079.1

Lutjeharms, J. R. E. (2006). *The Agulhas current*. Springer.

Lutjeharms, J. R. E. (2007). Three decades of research on the greater Agulhas Current. *Ocean Science*, *3*(1), 129–147. https://doi.org/10.5194/os-3-129-2007

Lutjeharms, J. R. E., Boebel, O., & Rossby, H. T. (2003). Agulhas cyclones. *Deep Sea Research Part II: Topical Studies in Oceanography*, *50*(1), 13–34. https://doi.org/10.1016/S0967-0645(02)00378-8

Lutjeharms, J. R. E., & Roberts, H. R. (1988). The Natal pulse: An extreme transient on the Agulhas Current. *Journal of Geophysical Research*, *93*(C1), 631–645. https://doi.org/10.1029/JC093iC01p00631

McMonigal, K., Beal, L., Elipot, S., Gunn, K., Hermes, J., Morris, T., & Houk, A. (2020). The impact of meanders, deepening and broadening, and seasonality on Agulhas current temperature variability. *Journal of Physical Oceanography*, *50*(12), 1–51. https://doi.org/10.1175/JPO-D-20-0018.1

Mitsudera, H., Waseda, T., Yoshikawa, Y., & Taguchi, B. (2001). Anticyclonic eddies and Kuroshio meander formation. *Geophysical Research Letters*, *28*(10), 2025–2028. https://doi.org/10.1029/2000GL012668

Miyazawa, Y., Guo, X., & Yamagata, T. (2004). Roles of mesoscale eddies in the Kuroshio paths. *Journal of Physical Oceanography*, *34*(10), 2203–2222. https://doi.org/10.1175/1520-0485(2004)034<2203:ROMEIT>2.0.CO;2

Morris, T., Aguiar-González, B., Ansorge, I., & Hermes, J. (2019). Lagrangian evolution of two Madagascar cyclonic eddies: Geometric properties, vertical structure, and fluxes. *Journal of Geophysical Research: Oceans*, *124*(11), 8193–8218. https://doi.org/10.1029/2019JC015090

Qiao, J., Qiu, C., Wang, D., Huang, Y., & Zhang, X. (2023). Multi-stage development within anisotropy insight of an anticyclone eddy in northwestern south China sea in 2021. *Geophysical Research Letters*, *50*(19), e2023GL104736. https://doi.org/10.1029/2023GL104736

Quartly, G. D., Buck, J. J. H., Srokosz, M. A., & Coward, A. C. (2006). Eddies around Madagascar — The retroflection re-considered. *Journal of Marine Systems*, *63*(3–4), 115–129. https://doi.org/10.1016/j.jmarsys.2006.06.001

Ridderinkhof, H., van Der Werf, P. M., Ullgren, J. E., van Aken, H. M., van Leeuwen, P. J., & de Ruijter, W. P. M. (2010). Seasonal and interannual variability in the Mozambique Channel from moored current observations. *Journal of Geophysical Research*, *115*(C6), C06010. https://doi.org/10.1029/2009JC005619

Ridderinkhof, W., Le Bars, D., von der Heydt, A. S., & de Ruijter, W. P. M. (2013). Dipoles of the south east Madagascar current. *Geophysical Research Letters*, *40*(3), 558–562. https://doi.org/10.1002/grl.50157

Rouault, M., & Penven, P. (2011). New perspectives on Natal Pulses from satellite observations. *Journal of Geophysical Research*, *116*(C7), 2010JC006866. https://doi.org/10.1029/2010JC006866

Russo, C. S., Lamont, T., & Krug, M. (2021). Spatial and temporal variability of the Agulhas Retroflection: Observations from a new objective detection method. *Remote Sensing of Environment*, *253*, 112239. https://doi.org/10.1016/j.rse.2020.112239

Russo, C. S., Veitch, J., Carr, M., Fearon, G., & Whittle, C. (2022). An intercomparison of global reanalysis products for southern Africa's major oceanographic features. *Frontiers in Marine Science*, *9*, 837906. https://doi.org/10.3389/fmars.2022.837906

Schouten, M. W., de Ruijter, W. P. M., & van Leeuwen, P. J. (2002). Upstream control of Agulhas ring shedding. *Journal of Geophysical Research*, *107*(C8), 3109. https://doi.org/10.1029/2001JC000804

Schouten, M. W., de Ruijter, W. P. M., van Leeuwen, P. J., & Ridderinkhof, H. (2003). Eddies and variability in the Mozambique channel. *Deep Sea Research Part II: Topical Studies in Oceanography*, *50*(12–13), 1987–2003. https://doi.org/10.1016/S0967-0645(03)00042-0

Schumann, E. H. (1981). Low frequency fluctuations off the Natal coast. *Journal of Geophysical Research*, *86*(C7), 6499–6508. https://doi.org/10.1029/JC086iC07p06499

Sheremet, V. A., Kamenkovich, V. M., & Pastushkov, A. R. (1995). Analysis of the barotropic model of the subtropical gyre in the ocean for finite Reynolds numbers. Part II. *Journal of Marine Research*, *53*(6), 995–1024. https://doi.org/10.1357/0022240953212945

Sheu, W.-J., Wu, C.-R., & Oey, L.-Y. (2010). Blocking and westward passage of eddies in the Luzon strait. *Deep Sea Research Part II: Topical Studies in Oceanography*, *57*(19), 1783–1791. https://doi.org/10.1016/j.dsr2.2010.04.004

Shi, Y., Yang, D., & He, Y. (2021). Numerical study on interaction between eddies and the Kuroshio Current east of Taiwan, China. *Journal of Oceanology and Limnology*, *39*(2), 388–402. https://doi.org/10.1007/s00343-020-0010-0

Stewart, K. D., Spence, P., Waterman, S., Sommer, J. L., Molines, J.-M., Lilly, J. M., & England, M. H. (2015). Anisotropy of eddy variability in the global ocean. *Ocean Modelling*, *95*, 53–65. https://doi.org/10.1016/j.ocemod.2015.09.005

Stramma, L., & Lutjeharms, J. R. E. (1997). The flow field of the subtropical gyre of the South Indian Ocean. *Journal of Geophysical Research*, *102*(C3), 5513–5530. https://doi.org/10.1029/96JC03455

Tsugawa, M., & Hasumi, H. (2010). Generation and growth mechanism of the natal pulse. *Journal of Physical Oceanography*, *40*(7), 1597–1612. https://doi.org/10.1175/2010JPO4347.1

van der Vaart, P. C. F., & de Ruijter, W. P. M. (2001). Stability of western boundary currents with an application to Pulselike behavior of the Agulhas current. *Journal of Physical Oceanography*, *31*(9), 2625–2644. https://doi.org/10.1175/1520-0485(2001)031<2625:SOWBCW>2.0.CO;2

van Aken, H. M., Lutjeharms, J. R. E., Rouault, M., Whittle, C., & de Ruijter, W. P. M. (2013). Observations of an early Agulhas current retroflection event in 2001: A temporary cessation of inter-ocean exchange south of Africa? *Deep Sea Research Part I: Oceanographic Research Papers*, *72*, 1–8. https://doi.org/10.1016/j.dsr.2012.11.002

Vandermeirsch, F. O., Carton, X. J., & Morel, Y. G. (2003). Interaction between an eddy and a zonal jet: Part I. One-and-a-half-layer model. *Dynamics of Atmospheres and Oceans*, *36*(4), 247–270. https://doi.org/10.1016/S0377-0265(02)00065-9

van Leeuwen, P. J., de Ruijter, W. P. M., & Lutjeharms, J. R. E. (2000). Natal pulses and the formation of Agulhas rings. *Journal of Geophysical Research*, *105*(C3), 6425–6436. https://doi.org/10.1029/1999JC900196

van Sebille, E., Beal, L. M., & Biastoch, A. (2010). Sea surface slope as a proxy for Agulhas Current strength. *Geophysical Research Letters*, *37*(9). https://doi.org/10.1029/2010GL042847

Wang, H., Qiu, B., Liu, H., & Zhang, Z. (2023). Doubling of surface oceanic meridional heat transport by non-symmetry of mesoscale eddies. *Nature Communications*, *14*(1), 5460. https://doi.org/10.1038/s41467-023-41294-7

Waseda, T., Mitsudera, H., Taguchi, B., & Yoshikawa, Y. (2002). On the eddy-Kuroshio interaction: Evolution of the mesoscale eddy. *Journal of Geophysical Research*, *107*(C8), 3-1-3–19. https://doi.org/10.1029/2000JC000756

Waseda, T., Mitsudera, H., Taguchi, B., & Yoshikawa, Y. (2003). On the eddy-Kuroshio interaction: Meander formation process. *Journal of Geophysical Research*, *108*(C7). https://doi.org/10.1029/2002JC001583

Waterman, S., & Hoskins, B. (2013). Eddy shape, orientation, propagation, and mean flow feedback in western boundary current jets. *Journal of Physical Oceanography*, *43*(8), 1666–1690. https://doi.org/10.1175/JPO-D-12-0152.1

Waterman, S., & Lilly, J. M. (2015). Geometric decomposition of eddy feedbacks in barotropic systems. *Journal of Physical Oceanography*, *45*(4), 1009–1024. https://doi.org/10.1175/JPO-D-14-0177.1

Yamagami, Y., Tozuka, T., & Qiu, B. (2019). Interannual variability of the natal pulse. *Journal of Geophysical Research: Oceans*, *124*(12), 9258–9276. https://doi.org/10.1029/2019JC015525

Yan, X., Kang, D., Pang, C., Zhang, L., & Liu, H. (2022). Energetics analysis of the eddy–Kuroshio interaction east of Taiwan. *Journal of Physical Oceanography*, *52*(4), 647–664. https://doi.org/10.1175/JPO-D-21-0198.1

Yan, X., Zhu, X.-H., Pang, C., & Zhang, L. (2016). Effects of mesoscale eddies on the volume transport and branch pattern of the Kuroshio east of Taiwan. *Journal of Geophysical Research: Oceans*, *121*(10), 7683–7700. https://doi.org/10.1002/2016JC012038

Yang, Y., & Liang, X. S. (2019). The intrinsic nonlinear multiscale interactions among the mean flow, low frequency variability and mesoscale eddies in the Kuroshio region. *Science China Earth Sciences*, *62*(3), 595–608. https://doi.org/10.1007/s11430-018-9289-4

Zhang, D., Lee, T. N., Johns, W. E., Liu, C.-T., & Zantopp, R. (2001). The Kuroshio east of Taiwan: Modes of variability and relationship to interior ocean mesoscale eddies. *Journal of Physical Oceanography*, *31*(4), 1054–1074. https://doi.org/10.1175/1520-0485(2001)031<1054:TKEOTM>2.0.CO;2

Zhang, Z., Qiu, B., Klein, P., & Travis, S. (2019). The influence of geostrophic strain on oceanic ageostrophic motion and surface chlorophyll. *Nature Communications*, *10*(1), 2838. https://doi.org/10.1038/s41467-019-10883-w

Zhu, Y., Qiu, B., Lin, X., & Wang, F. (2018). Interannual eddy kinetic energy modulations in the Agulhas return current. *Journal of Geophysical Research: Oceans*, *123*(9), 6449–6462. https://doi.org/10.1029/2018JC014333